

# Near-wall effect on flow around an elliptic cylinder translating above a plane wall

Cite as: Phys. Fluids **32**, 093607 (2020); <https://doi.org/10.1063/5.0020818>

Submitted: 06 July 2020 . Accepted: 29 August 2020 . Published Online: 18 September 2020

Jianxun Zhu , Lars Erik Holmedal , Dag Myrhaug , and Hong Wang 



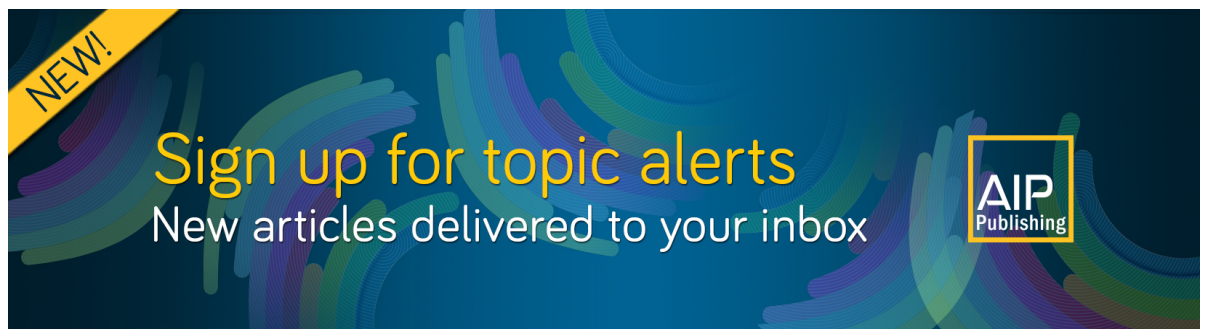
View Online



Export Citation




CrossMark



**NEW!**

Sign up for topic alerts  
New articles delivered to your inbox



# Near-wall effect on flow around an elliptic cylinder translating above a plane wall

Cite as: Phys. Fluids 32, 093607 (2020); doi: 10.1063/5.0020818

Submitted: 6 July 2020 • Accepted: 29 August 2020 •

Published Online: 18 September 2020



View Online



Export Citation



CrossMark

Jianxun Zhu,<sup>a)</sup>  Lars Erik Holmedal,  Dag Myrhaug,  and Hong Wang 

## AFFILIATIONS

Department of Marine Technology, Norwegian University of Science and Technology, 7491 Trondheim, Norway

<sup>a)</sup> Author to whom correspondence should be addressed: [jianxun.zhu@ntnu.no](mailto:jianxun.zhu@ntnu.no)

## ABSTRACT

In this work, the flow over an elliptic cylinder near a moving wall is investigated for Reynolds numbers less than 150. Here, the ratio between the gap (i.e., the distance between the cylinder and the wall) and the length of the semi-major axis of the elliptic cylinder varies from 0.1 to 5. This ratio is hereafter denoted as the gap ratio. The resulting Kármán vortex street, the two-layered wake, and the secondary vortex street have been investigated and visualized. Numerical simulations show that for the steady flow, the wake is composed of two asymmetric recirculation vortices, while a decrease in the gap ratio suppresses the vortex shed from the lower part of the cylinder. For the unsteady flow, the wake can be classified into four different patterns based on the wake structures (the Kármán vortex street, the two-layered wake, and the secondary vortex street). The regions of these wake patterns are given in the gap ratio and Reynolds number space, showing that the critical Reynolds number for the transition between different patterns increases as the gap ratio decreases. An overall increase in the mean drag coefficient with increasing gap ratios is observed, except for a sudden drop that occurs within a small gap ratio range. Moreover, as the gap ratio increases, the onset location of the two-layered wake first decreases due to a decrease in flow velocity in the gap and then increases due to the weakening of the wall suppression effect.

Published under license by AIP Publishing. <https://doi.org/10.1063/5.0020818>

## I. INTRODUCTION

The wake behind an isolated circular cylinder has been studied extensively because of its vital importance in understanding vortex shedding in engineering applications, such as marine risers and bridges. At low Reynolds numbers (based on the cylinder diameter and the free-stream velocity), the flow is symmetrical around the cylinder without flow separation. As the Reynolds number increases to about 7, laminar separation occurs, forming a pair of counter-rotating vortices, which are symmetrical about the centerline of the wake,<sup>1,2</sup> and as the Reynolds number increases further, the well-known Kármán vortex street is formed.<sup>3,4</sup> This vortex street exhibits a transition to a two-layered wake farther downstream, followed by a second transition (even farther downstream) to a secondary vortex street with larger spatial scales than the primary ones.<sup>5</sup> The physical mechanism underpinning the formation of the two-layered wake was investigated experimentally by Durgin and Karlsson<sup>6</sup> and Karasudani and Funakoshi.<sup>7</sup> They measured the vertical distance ( $h$ ) between the upper and lower wake vortices and the horizontal distance ( $l$ ) between two successive co-rotating vortices along the wake

and found that the ratio ( $h/l$ ) between these vertical and horizontal distances increases downstream. At a given downstream location, this ratio reaches a critical value where two successive vortices shed from the upper part of the cylinder impose the convection of vorticity within the vortex shed from the lower part of the cylinder. This vortex is located horizontally in between the two upper vortices (and vice versa if the two successive vortices shed from the lower part of the cylinder). As a result, this vortex starts to distort and rotate to align with the stream-wise direction, forming the two-layered wake.

Experiments conducted by Cimbalá *et al.*<sup>5</sup> showed the broad-band frequency spectra of the vertical velocity fluctuation in the far wake. For Reynolds numbers between 100 and 160, the broad-band spectra contain several prominent frequencies considerably lower than the Kármán shedding frequency. It appears to be a strong correlation between these low frequencies and the secondary vortex street, which contains vortices with spatial scales larger than the Kármán vortices. In the view of this, Cimbalá *et al.*<sup>5</sup> attributed the formation for the secondary vortex street to the hydrodynamic instability of the mean wake. This hypothesis was supported by Kumar and

Mittal<sup>8</sup> who conducted two-dimensional numerical simulations of the flow around an isolated circular cylinder for a Reynolds number of 150. Here, packets of fluctuating vortices (i.e., based on the fluctuating velocity field) with a range of spatial scales were formed in the far wake, and these vortex packets grew stronger (i.e., contained larger vorticity) through convection. On this basis, Kumar and Mittal<sup>8</sup> argued that the transition from the two-layered wake to the secondary vortex street is due to the convective instability of the mean wake flow. Matsui and Okude<sup>9</sup> conducted experimental measurements for the flow around an isolated circular cylinder for Reynolds numbers less than 160 and explained the formation of the secondary vortex street in terms of merging of Kármán vortices. They also found that when the wake was forced acoustically by one-half and one-third of the Kármán shedding frequency, two and three of vortices merged into a large secondary vortex, respectively. The explanation of this behavior, as demonstrated by Williamson and Prasad<sup>10</sup> in their experiments for Reynolds numbers less than 170, is that the far wake flow is sensitive to the perturbation of the free-stream velocity. A very small perturbation of the free-stream velocity can lead to visible spectral peaks with the perturbation frequency and with the frequency difference between the Kármán shedding and the perturbation. Recently, Jiang and Cheng<sup>11</sup> investigated unforced (uniform inlet velocity without perturbations) cylinder wakes using two-dimensional numerical simulations and found two formation mechanisms for the secondary vortex street: (i) the merging of two co-rotating vortices for Reynolds numbers ranging from 200 to 300 and (ii) the pairing of two counter-rotating vortices, followed by the merging of these paired vortices for Reynolds numbers ranging from 400 to 1000.

Wakes behind other bluff bodies such as square<sup>12,13</sup> and elliptic cylinders have been investigated due to the practical impact on submarines<sup>14</sup> and heat exchangers.<sup>15</sup> For elliptic cylinders, the flow depends on both the aspect ratio ( $AR$ ) of the elliptic cylinder (defined by the ratio of the semi-minor to semi-major axis length) and the incident angle (defined by the angle between the inlet flow direction and the semi-minor axis) in addition to the Reynolds number based on the free-stream velocity and the semi-major axis length. Johnson *et al.*<sup>16</sup> used two-dimensional numerical simulations to investigate the flow around an isolated elliptic cylinder of aspect ratios ranging from 0.01 to 1 (i.e., from a flat plate to a circular cylinder) for Reynolds numbers up to 200 at zero incident angle. They found that for an aspect ratio of 0.5, the flow is steady for a Reynolds number of 40, while Kármán vortex shedding exists for a Reynolds number of 75. As the Reynolds number increases further to 125, the Kármán vortex street is followed by a two-layered wake (farther downstream); as the Reynolds number increases even further to 150, the secondary vortex street is formed in the far wake. This secondary vortex street moves upstream and becomes more irregular as the Reynolds number increases up to 200. The critical Reynolds number for the onset of the Kármán vortex street, the two-layered wake, and the secondary vortex street in the wake increases as the aspect ratio increases. Johnson *et al.*<sup>17</sup> investigated the power spectrum numerically of the vertical velocity along the horizontal centerline downstream of the cylinder, revealing the presence of secondary and tertiary frequencies in the far wake. These frequencies are lower than the Kármán shedding frequency. The peaks of the power spectrum at these low frequencies become larger farther downstream, triggering the transition from the two-layered

wake to the secondary vortex street. Raman *et al.*<sup>18</sup> conducted two-dimensional simulations for the flow around an elliptic cylinder with aspect ratios from 1 to 10 for Reynolds numbers from 50 to 500. They found that the vortex shedding can be suppressed by increasing the aspect ratio for a given Reynolds number. Yoon *et al.*<sup>19</sup> and Paul *et al.*<sup>20</sup> found that the critical Reynolds number for the vortex shedding suppression decreases as the angle of attack increases from  $0^\circ$  to  $90^\circ$ . Subburaj *et al.*<sup>21</sup> used the immersed boundary method and the level set method to investigate the two-dimensional flow around the elliptic cylinder with aspect ratios of 0.25 and 0.5 near a free surface for a Reynolds number of 180 with different angles of attack, showing that for a submergence depth of 0.096, the vortex shedding is suppressed at the angle of attack of  $45^\circ$ , while metastable states appear at  $-45^\circ$ , and at  $90^\circ$ , vortex shedding is partially suppressed.

Transitional movements of bluff bodies near a stationary plane wall are both important in academic research and engineering applications, such as submarines or AUV (Autonomous Underwater Vehicle) moving near a seabed. The latter is of great importance for inspections of subsea structures as well as for mapping of the ocean bathymetry and collection of both physical data (e.g., of wave-induced velocities, current velocities, and sediment concentration) and biological data (e.g., fish larvae, plankton, and contamination). Taneda<sup>22</sup> and Zdravkovich<sup>23</sup> towed a circular cylinder along a plane wall in a water tank for Reynolds numbers of 170 and 3550 and found alternating vortices shed from the upper and lower parts of the cylinder with a gap-to-diameter ratio of 0.6. When the same experiment was conducted for a gap-to-diameter ratio of 0.1, only a single row of vortices was shed from the upper part of the cylinder. Huang and Sung<sup>24</sup> conducted two-dimensional numerical simulations, finding that for a Reynolds number of 300, the flow exhibits (i) a Kármán-like vortex shedding at a gap-to-diameter ratio of 0.6; (ii) a pair-wise vortex shedding, where the lift and drag forces fluctuate with the same frequency at a gap-to-diameter ratio of 0.2; and (iii) a single row of vortex shedding from the upper part of the cylinder at a gap-to-diameter ratio of 0.1. The drag force increases as the gap-to-diameter ratio increases (for a given Reynolds number) up to a critical value (i.e., at the onset of the Kármán-like vortex shedding) where the drag force reaches its maximum value. As the gap-to-diameter ratio increases further, the drag force decreases. It appears that the drag force is closely correlated with the base pressure<sup>25</sup> (i.e., the lowest pressure located at the downstream side of the cylinder). As the gap-to-diameter ratio increases up to the critical value, the vortices behind the cylinder become stronger due to the weakening of the wall suppression effect, thus drawing in fluid at a higher rate<sup>26</sup> resulting in a lower base pressure and a larger drag force. As the gap-to-diameter ratio increases beyond this critical value, stronger vortices are shed from the bottom of the cylinder, resulting in an enhanced interaction with the vortices shed from the top of the cylinder, causing a higher vortex shedding frequency. This implies a shorter time interval for the vortices to grow before they move downstream, resulting in weaker vortices, which again cause a larger base pressure and a smaller drag force.<sup>25</sup> Moreover, as the gap-to-diameter ratio decreases (for a given Reynolds number), the stagnation point at the front of the cylinder moves downward along the cylinder, causing a more asymmetric flow distribution around the cylinder, resulting in a larger lift force.<sup>25</sup> Jiang *et al.*<sup>27</sup> conducted a comprehensive set of numerical investigations of the two- and

three-dimensional wake transitions for Reynolds numbers up to 300 at gap-to-diameter ratios between 0.1 and 19.5. They found that for flow in the two-dimensional regime, the critical Reynolds number for the onset of the vortex shedding increases as the gap-to-diameter ratio decreases. This behavior further confirms that the presence of the wall weakens the interaction between the vortices shed from the top and bottom parts of the cylinder, thus delaying the vortex shedding.

The development of the Kármán vortex street, the two-layered wake, and the secondary vortex street behind isolated cylinders has been investigated previously for a wide range of Reynolds numbers and aspect ratios. Paul *et al.*<sup>20</sup> showed that the critical Reynolds number for the onset of the flow separation and the Kármán vortex shedding decreases with the decreasing aspect ratios. Johnson *et al.*<sup>16</sup> found that the critical Reynolds number for the onset of the two-layered wake and the secondary vortex street decreases with the decreasing gap ratio. Thompson *et al.*<sup>28</sup> found that an increase in Reynolds number for a given gap ratio or a decrease in gap ratios for a given Reynolds numbers results in the onset location of the two-layered wake and the secondary vortex street (which becomes more irregular) being closer to the cylinder. Moreover, Jiang *et al.*<sup>27</sup> showed that the presence of a moving wall has a significant effect on the flow around a near-wall circular cylinder, e.g., suppressing the Kármán vortex shedding and changing the lift and drag coefficients by varying the gap ratio. However, the effect of a moving wall on the two-layered wake and the secondary vortex street behind a near-wall elliptic cylinder with an aspect ratio less than 1 has not been investigated previously. This is presented in the present work, together with the resulting forces on the elliptic cylinder itself.

Specifically, the flow over an elliptic cylinder with the aspect ratio of 0.4 near a moving wall is investigated for Reynolds numbers less than 150. Here, the ratio between the gap (i.e., the distance between the cylinder and the wall) and the length of the semi-major axis of the elliptic cylinder varies from 0.1 to 5. The resulting Kármán vortex street, the two-layered wake, and the secondary vortex street have been investigated and visualized. Numerical simulations show that for the steady flow, the wake is composed of either two asymmetric recirculation vortices or one recirculation vortex behind the cylinder; for the unsteady flow, the wake can be classified into four different patterns based on the wake structures. These wake patterns are mapped out in the gap ratio and Reynolds number space, and a detailed analysis of the near-wall effect (i.e., the effect of the gap ratios) on the lift and drag coefficients as well as on the onset location of the two-layered wake is presented.

## II. PROBLEM DEFINITION AND GOVERNING EQUATIONS

The current paper addresses the flow around an elliptic cylinder moving parallel to a wall with a constant velocity. It is convenient for numerical simulations to use a uniformly translating frame of reference fixed on the cylinder such that the cylinder is stationary, while the wall and the fluid move toward the right at a uniform speed, as shown in Fig. 1. The aspect ratio ( $AR$ ) of the cylinder is defined by the minor ( $a$ ) to major ( $D$ ) axis length ratio, i.e.,  $AR = a/D$ . The gap ratio is given by  $G/D$ , where  $G$  is the gap between the moving wall and the cylinder, and the Reynolds number is based on the major

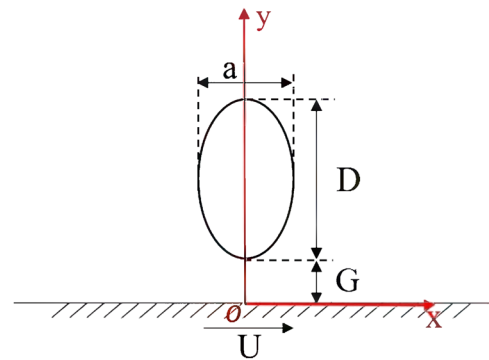


FIG. 1. Definition of relevant dimensions for the flow around an elliptic cylinder near a moving wall.

axis, i.e.,  $Re = UD/\nu$ , where  $\nu$  is the kinematic viscosity. Here, the incompressible flow with a constant density  $\rho$  is governed by the dimensionless two-dimensional Navier–Stokes equations given as

$$\frac{\partial u_i}{\partial x_i} = 0, \quad (1)$$

$$\frac{\partial u_i}{\partial t} + \frac{\partial u_i u_j}{\partial x_j} = -\frac{\partial p}{\partial x_i} + \frac{1}{Re} \frac{\partial^2 u_i}{\partial x_j \partial x_j}, \quad (2)$$

where the Einstein notation using the repeated indices is applied. Here,  $u_i = (u, v)$  and  $x_i = (x, y)$  for  $i = 1$  and 2 indicate the velocity and Cartesian coordinates, respectively, while  $t$  and  $p$  denote the time and pressure, respectively. The velocity, time, pressure, and length are scaled by  $U$ ,  $D/U$ ,  $\rho U^2$ , and  $D$ , respectively.

## III. NUMERICAL METHODS

A projection method is used for solving Eqs. (1) and (2). The convective terms and the diffusive terms are discretized by Adams–Bashforth and Crank–Nicolson schemes, respectively. The spatial derivatives are discretized with a second-order centered finite difference scheme on a staggered grid arrangement. The Poisson equation for pressure correction is solved using a biconjugate gradient stabilized method (BiCGSTAB)<sup>29</sup> with a Jacobi preconditioner.

The cylinder geometry is taken into account by a direct-forcing immersed boundary method.<sup>30</sup> Figure 2 shows the treatment of the Cartesian grid and the immersed boundary. A grid cell is blocked out of the simulation if its corresponding variable (velocity or pressure) lies within the immersed boundary. Then, the velocity point at the cell face between a blocked cell and an unblocked cell is set as an inactive velocity (■), which are updated by interpolation using the physical boundary condition at the immersed boundary point (○) and the active velocity point (□) within the fluid. Here, weighted one-dimensional, cubic Lagrange interpolation schemes are applied as follows:

$$f(x) = \sum_{k=1}^3 \beta_k(x) f_k + \beta(x_\Gamma) f_\Gamma, \quad (3)$$

where  $x$  and  $x_\Gamma$  denote the locations of the inactive point and the immersed boundary, respectively, while  $f(x)$ ,  $f_k$ , and  $f_\Gamma$

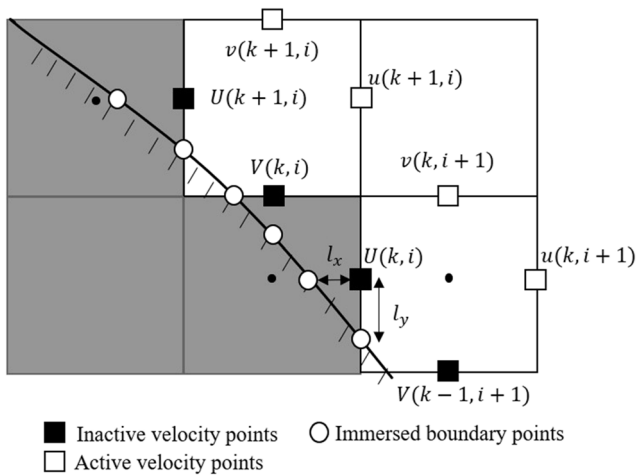


FIG. 2. Definition of the inactive velocity points (■), immersed boundary points (○), and active velocity points (□).

represent the velocity values at the inactive points, the active velocity points, and the immersed boundary, respectively. Here, the Lagrange coefficients  $\beta_k(x)$  and  $\beta(x_\Gamma)$  can be obtained by

$$\beta_k(x) = \left( \prod_{j=1, j \neq k}^3 \frac{(x - x_j)}{(x_k - x_j)} \right) \frac{x - x_\Gamma}{x_k - x_\Gamma}, \quad (4)$$

$$\beta(x_\Gamma) = \left( \prod_{j=1}^3 \frac{(x - x_j)}{(x_\Gamma - x_j)} \right), \quad (5)$$

where  $x_j$  denote the location of the  $j$ th active point.

If an inactive velocity point can be interpolated from two directions, each direction is multiplied by a weighting factor as follows:

$$f(x) = \lambda_x f^x + \lambda_y f^y, \quad (6)$$

where the superscripts  $x$  and  $y$  denote the interpolation in the  $x$  and  $y$  directions, respectively, and the weighting factors  $\lambda_x$  and  $\lambda_y$  are given as

$$\lambda_x = \frac{1}{1 + (\frac{l_x}{l_y})^2} \quad \text{and} \quad \lambda_y = \frac{1}{1 + (\frac{l_y}{l_x})^2}, \quad (7)$$

where  $l_x$  and  $l_y$  are the distances between the inactive point and the immersed boundary in the  $x$  and  $y$  directions, respectively, as shown in Fig. 2. Moreover, a Neumann condition for the pressure correction is applied at the inactive velocity points.

#### IV. VALIDATION AGAINST PREVIOUS NUMERICAL AND EXPERIMENTAL RESULTS

Numerical investigations of the two-dimensional flow around an isolated circular cylinder are conducted for  $Re = 40, 100,$  and  $200$ . A dimensionless free-stream velocity  $U = 1$  is specified at the inlet boundary, while a Neumann condition is imposed for the velocity at the outlet and lateral boundaries. A no-slip condition is applied at the cylinder. The pressure is set to be zero at the outlet, and a Neumann condition for the pressure correction is imposed at the other boundaries. A spin-up time of  $t = t^* U/D = 200$  (where  $t^*$  is the physical time) was found to be sufficient to obtain a fully developed flow for all the cases. For  $Re = 40$ , the flow reaches a steady state where two counter-rotating vortices, which are symmetrical about the centerline of the wake, are formed [see Fig. 3(a)]; for  $Re = 100$  and  $200$ , the flow exhibits an unsteady state where periodic alternating vortex shedding (Kármán vortices) occurs as visualized by the streamlines in Figs. 3(b) and 3(c), respectively.

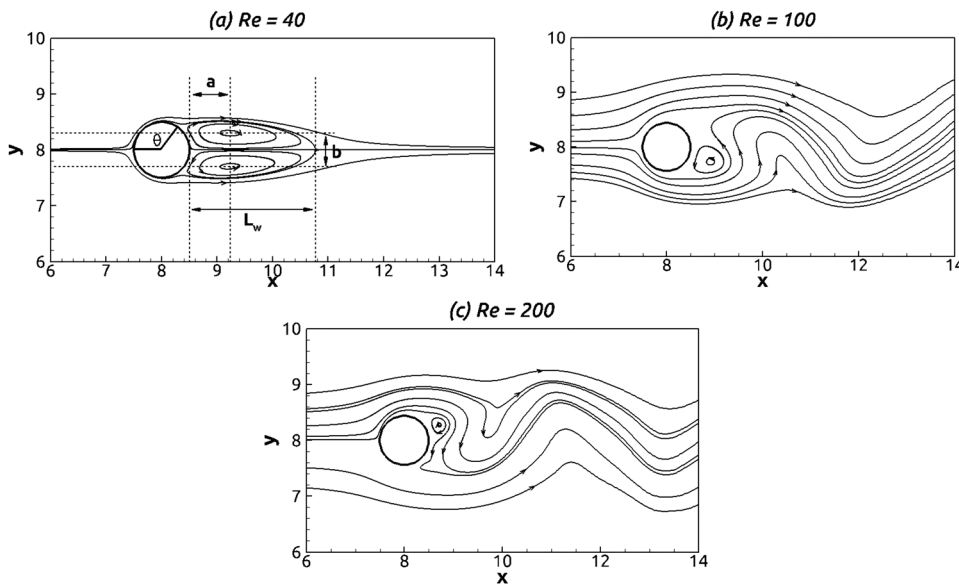


FIG. 3. Streamlines for the flow over a cylinder at  $Re =$  (a) 40, (b) 100, and (c) 200 as well as the nomenclature used in Table I. Separation angle  $\theta$ , wake length  $L_w$ , horizontal distance  $a$  between the rear stagnation point of the cylinder and the recirculation center, and vertical distance  $b$  between the symmetric recirculation centers.

**TABLE I.** The physical parameters obtained by the present numerical method and previous works for the flow around a circular cylinder at  $Re = 40$ ; the superscript \* denotes that the results were obtained by experiments. The front stagnation point is located at  $\theta = 180^\circ$ .

|  | $C_D$ | $\theta$ (deg) | $L_w$ | $a$  | $b$  |
|--|-------|----------------|-------|------|------|
| *Coutanceau and Bouard <sup>31</sup>   |       | 53.8           | 2.13  | 0.76 | 0.59 |
| Linnick and Fasel <sup>32</sup>        | 1.54  | 53.6           | 2.28  | 0.72 | 0.60 |
| Fornberg <sup>33</sup>                 | 1.50  | 55.6           | 2.24  |      |      |
| Patil and Lakshmis <sup>34</sup>       | 1.56  | 52.7           | 2.14  |      |      |
| Taira and Colonius <sup>35</sup>       | 1.54  | 53.7           | 2.30  | 0.73 | 0.60 |
| Berthelsen and Faltinsen <sup>36</sup> | 1.59  | 53.9           | 2.29  | 0.72 | 0.60 |
| Coarse mesh (0.02)                     | 1.57  | 52.5           | 2.26  | 0.72 | 0.60 |
| Fine mesh (0.01)                       | 1.59  | 53.1           | 2.26  | 0.72 | 0.60 |

The inlet is located 8 cylinder diameters upstream of the cylinder center, the outlet is located 20 diameters downstream of the cylinder center, while the top and bottom boundaries are located 10 diameters away from the cylinder center. A fine uniform grid ( $\Delta x = \Delta y = 0.01$ , where  $\Delta x$  and  $\Delta y$  represent the length and the width of a grid cell, respectively) is applied in a small square region around the cylinder (i.e.,  $-0.7 \leq x \leq 0.7$  and  $-0.7 \leq y \leq 0.7$ ). From the edges of this region, the grid is stretched (using geometric series) in both the horizontal and vertical directions using stretch ratios less than 1.05.

Table I shows comparisons between the results obtained in the present work and the available results obtained from experiments<sup>31</sup> and numerical simulations for  $Re = 40$ .<sup>32-36</sup> Here,  $C_D$  is the drag coefficient;  $\theta$ ,  $L_w$ ,  $a$ , and  $b$  (as shown in Fig. 3) denote the separation angle, wake length, the horizontal distance between the rear stagnation point of the cylinder and the recirculation center, and the vertical distance between the symmetric recirculation centers, respectively. The drag coefficient  $C_D$  is defined as  $C_D = 2F_d/(\rho U^2 D)$ , where  $F_d$  is the drag force acting on the cylinder in the x direction. The wake parameters  $L_w$ ,  $a$ , and  $b$  are scaled by the diameter of the cylinder. Table I shows that a good agreement is obtained with the previous experimental<sup>31</sup> and numerical<sup>32-36</sup> results.

Table II shows comparisons between the present results and the available results obtained from the experiments<sup>37</sup> and the numerical simulations<sup>36,38-41</sup> for  $Re = 100$  and 200. The quantities that are compared are the time-averaged drag coefficient ( $\overline{C_D}$ ), the Strouhal number  $St = Df/U$  (where  $f$  represents the vortex shedding frequency), the lift coefficient amplitude [ $C_{l,a}$ , where  $C_l = 2F_l/(\rho U^2 D)$ , with  $F_l$  being the lift force], and the drag coefficient amplitude ( $C_{D,a}$ ). The present results are in good agreement with those obtained by Berthelsen and Faltinsen<sup>36</sup> who used an immersed boundary method similar to the present method. Overall, the present results are in fair to good agreement with those presented in Table II.

A grid refinement test was conducted using a coarse grid ( $\Delta x = \Delta y = 0.02$ ) in the small rectangular domain around the cylinder, and then stretching the grid vertically and horizontally from the edges of this domain. The deviation from the results obtained with the fine grid was less than 1.2% for the quantities given in Tables I and II.

### V. RESULTS AND DISCUSSION

Numerical investigations of the flow around an elliptic cylinder with an aspect ratio  $AR = 0.4$  near a moving wall have been conducted for  $Re$  ranging from 30 to 150 for gap ratios  $G/D$  ranging from 0.1 to 5. Figure 4 shows the computational domain, the location of the cylinder, and the boundary conditions. The inlet and top boundaries are located  $20D$  away from the cylinder center, the outlet is located  $50D$  downstream of the cylinder center, and the bottom boundary is located  $(G/D + 0.5)D$  from the cylinder center. A dimensionless velocity  $u = 1$  is set at the inlet, and a Neumann condition is imposed for the velocity at the top and outlet boundaries. A no-slip condition is applied at the cylinder and the bottom wall, which moves toward the right at  $u = 1$ . The pressure is equal to zero at the outlet, and a Neumann condition for the pressure correction is imposed at other boundaries.

A uniform grid ( $\Delta x = \Delta y = 0.02$ ) is applied to a region (marked by a blue rectangle in Fig. 4) around the cylinder. The edges of this region are located  $0.7D$  away from the cylinder center. The grid is stretched from the top and left edges of this edge using constant stretch ratios less than 1.02. From the right edge, the grid is stretched

**TABLE II.** Comparisons between present results and previous numerical and experimental results: Strouhal number  $St$ , lift coefficient amplitude  $C_{l,a}$ , drag coefficient  $C_D$ , and amplitude  $C_{D,a}$  for the uniform flow around a circular cylinder at  $Re = 100$  and 200; the superscript \* denotes that the results were obtained by experiments.

|  | $Re = 100$       |       |           |           | $Re = 200$       |       |           |           |
|--|------------------|-------|-----------|-----------|------------------|-------|-----------|-----------|
|  | $\overline{C_D}$ | $St$  | $C_{l,a}$ | $C_{D,a}$ | $\overline{C_D}$ | $St$  | $C_{l,a}$ | $C_{D,a}$ |
| *Williamson <sup>37</sup>              | ...              | 0.164 | ...       | ...       | ...              | 0.197 | ...       | ...       |
| Calhoun <sup>38</sup>                  | 1.33             | 0.175 | 0.298     | 0.014     | 1.17             | 0.202 | 0.668     | 0.058     |
| Russel and Wang <sup>39</sup>          | 1.38             | 0.169 | 0.300     | 0.007     | 1.29             | 0.195 | 0.500     | 0.022     |
| Xu and Wang <sup>40</sup>              | 1.42             | 0.171 | 0.340     | 0.013     | 1.42             | 0.202 | 0.660     | 0.040     |
| Berthelsen and Faltinsen <sup>36</sup> | 1.38             | 0.169 | 0.340     | 0.010     | 1.37             | 0.200 | 0.700     | 0.046     |
| Wang <i>et al.</i> <sup>41</sup>       | 1.38             | 0.170 | 0.357     | ...       | 1.26             | 0.195 | 0.708     | ...       |
| Coarse mesh (0.02)                     | 1.36             | 0.170 | 0.323     | 0.010     | 1.35             | 0.200 | 0.707     | 0.047     |
| Fine mesh (0.01)                       | 1.37             | 0.171 | 0.337     | 0.012     | 1.36             | 0.200 | 0.706     | 0.048     |

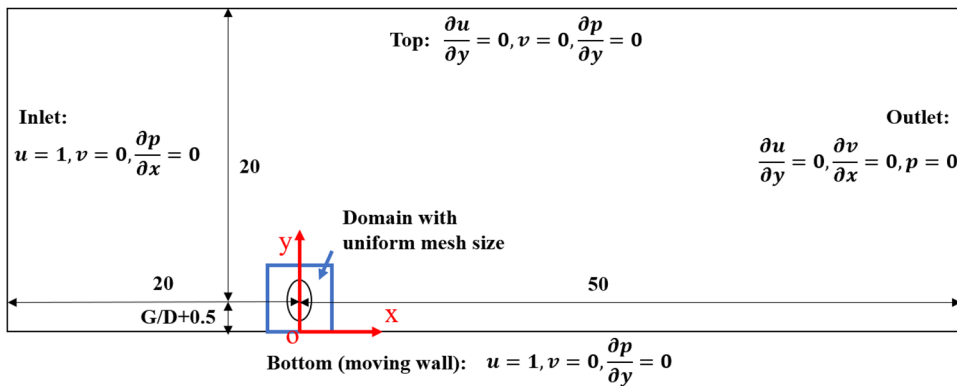


FIG. 4. Sketch of the computational domain and the boundary conditions for the flow around an elliptic cylinder near a moving wall.

over the next  $10D$  downstream (using a stretch ratio of 1.01) until  $\Delta x = 0.1$ , which is held constant over the rest of the downstream region. For gap ratios less than 1, the grids between the cylinder bottom and the bottom wall have the same vertical size, i.e.,  $\Delta y = 0.02$ . For gap ratios larger than 1, the grid is stretched symmetrically from the bottom wall and from the cylinder bottom to the center position between them using a stretching ratio less than 1.01. Figure 5 shows the complete grid for the whole computational domain and a close-up of the uniform grid around the cylinder for  $G/D = 0.2$ . For all the simulations conducted in this study, a spin-up time of  $t = 400$  was found to be sufficient to obtain a fully developed flow where the fluctuation amplitude and the period of  $C_D$  and  $C_l$  are fully developed, as exemplified in Fig. 6, showing the time history of  $C_D$  and  $C_l$  for  $Re = 150$  with  $G/D = 0.2$  and 2. This was checked for each simulation.

To test grid independence, numerical simulations were conducted using the coarse grid resolution and the fine grid resolution, as given in Table III for the largest Reynolds number  $Re = 150$  and the smallest gap ratio  $G/D = 0.1$ . Table III shows  $St$ ,  $\overline{C_D}$ , and  $\overline{C_l}$  obtained by the two grid resolutions, showing deviations of 0.9%, 0.6%, and 2.7%, respectively, from those obtained with the coarse grid. Thus, the coarse grid is sufficient to obtain the grid independent results.

### A. Steady state

The flow around an isolated elliptic cylinder with  $AR = 0.4$  is in the steady regime for  $Re = 30$ , while the vortex shedding occurs for  $Re = 40$ , as visualized by vorticity and streamline contours in Figs. 7(a) and 7(b), respectively. Here, the critical Reynolds number

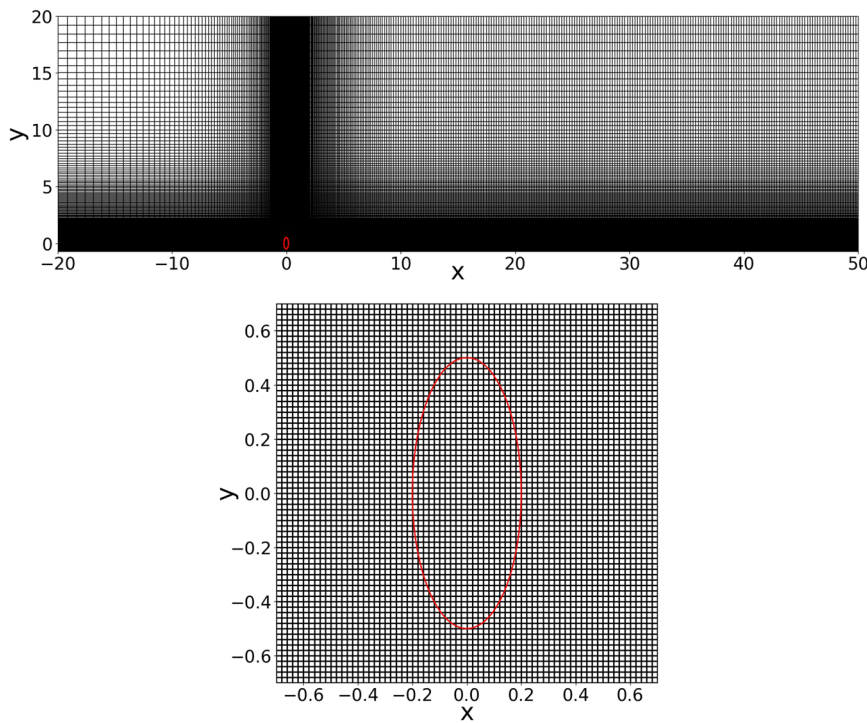
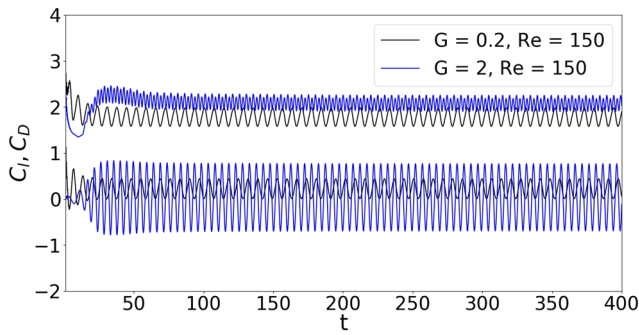


FIG. 5. Grid for the whole computational domain and a close-up of the uniform grid around the cylinder at  $G/D = 0.2$ .



**FIG. 6.** Time history of  $C_D$  (upper two curves) and  $C_l$  (lower two curves) for  $Re = 150$  with  $G/D = 0.2$  and  $2$ .

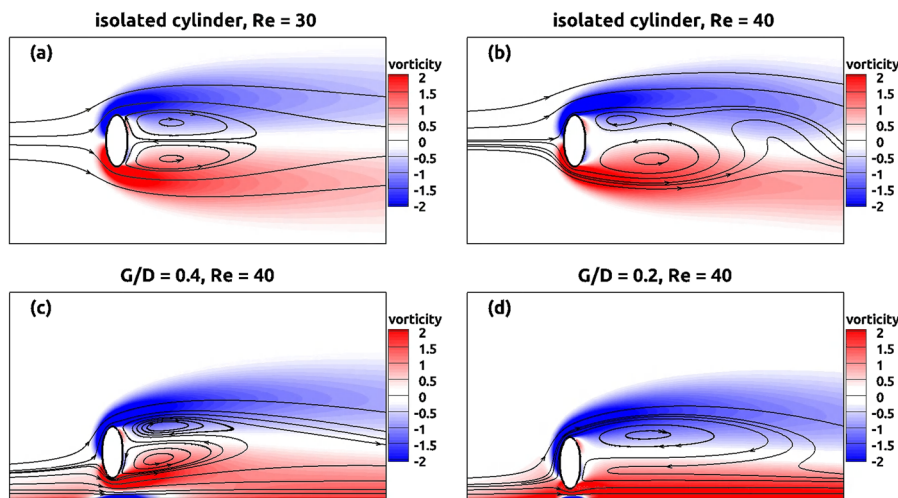
**TABLE III.** Comparisons of the  $St$ ,  $\overline{C}_D$ , and  $\overline{C}_l$  obtained by the computation domain 2 with the uniform mesh sizes  $\Delta x = \Delta y = 0.02$  and  $0.01$  for  $Re = 150$  and  $G/D = 0.1$ .

| Mesh size                               | $St$  | $\overline{C}_D$ | $\overline{C}_l$ |
|---|-------|------------------|------------------|
| Coarse ( $\Delta x = \Delta y = 0.02$ ) | 0.105 | 1.66             | 0.36             |
| Fine ( $\Delta x = \Delta y = 0.01$ )   | 0.106 | 1.67             | 0.35             |

$Re_c$  for the onset of the vortex shedding is  $35 \pm 5$ , which is smaller than the critical Reynolds number for a circular cylinder ( $AR = 1$ ) and ranges from 45 to 49,<sup>3,4,42</sup> a decrease in  $AR$  leads to a decrease in  $Re_c$ . The effect of the aspect ratio on the critical Reynolds number has been investigated numerically by Thompson *et al.*<sup>28</sup> and Paul *et al.*,<sup>20</sup> finding that  $Re_c$  decreases from 47.2 to 31.6 and from  $48.5 \pm 0.5$  to  $23.5 \pm 0.5$ , respectively, as  $AR$  decreases from 1 to 0.1. Thompson *et al.* obtained a larger  $Re_c$  for  $AR = 0.1$  than Paul *et al.* This is mainly because the blockage ratio of the grid system used by Thompson *et al.* is 1%, which is much smaller than 6.25% used by Paul *et al.*

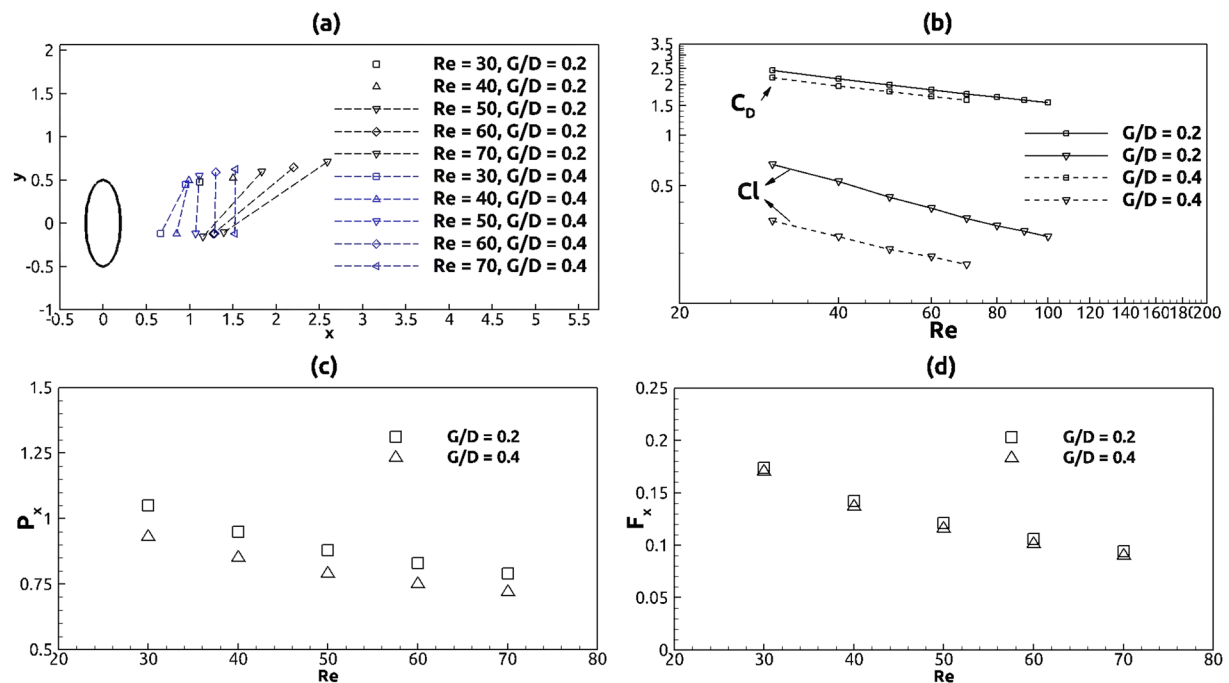
Figures 7(c) and 7(d) show the vorticity and streamline contours for  $Re = 40$  at  $G/D = 0.4$  and  $0.2$ , respectively. The flow reaches a steady state (i.e., no vortex shedding) at  $G/D = 0.4$  [Fig. 7(c)], while at the same  $Re$ , the flow exhibits vortex shedding for the isolated cylinder [Fig. 7(b)]. This is because the shear layer (negative vorticity) generated near the moving wall weakens the shear layer beneath the bottom of the cylinder (positive vorticity), thus delaying the onset of vortex shedding. This is the same mechanism as has been previously observed for a circular cylinder near a moving wall.<sup>27,43,44</sup> As  $G/D$  decreases further to  $0.2$ , the lower recirculation vortex as observed in Fig. 7(c) vanishes. The impact of  $G/D$  on the front stagnation point for a circular cylinder near a moving wall was investigated by Jiang *et al.*<sup>27</sup> using two-dimensional numerical simulations, showing that the front stagnation point moves downward along the cylinder as  $G/D$  decreases. This behavior is also observed in the present studies and is visualized by the streamlines in Figs. 7(c) and 7(d). It appears that more fluid moves upward along the cylinder due to the enhanced blockage effect in the gap [as can be seen by the downward movement of the front stagnation point in Figs. 7(c) and 7(d)] caused by decreasing  $G/D$ , forming a larger recirculation vortex for  $G/D = 0.2$  than for  $G/D = 0.4$ . This behavior is qualitatively similar to the observation by Jiang *et al.*<sup>27</sup> for the flow around a circular cylinder near a moving wall.

Figure 8(a) shows the recirculation vortex centers for  $Re$  ranging from 30 to 70 at  $G/D = 0.2$  and  $0.4$ , i.e., in the parameter range where the flow is steady. The upper recirculation vortex is formed for all the values of  $Re$  and  $G/D$  considered here, while the lower recirculation vortex disappears for  $Re \leq 40$  at  $G/D = 0.2$ . It appears that the lower recirculation vortex center is located closer to the cylinder than the upper recirculation vortex center, and this difference is larger for  $G/D = 0.2$  than for  $G/D = 0.4$  due to the stronger wall suppression effect on the lower recirculation vortex. For  $G/D = 0.4$ , an increase in  $Re$  leads to a smaller difference since thinner shear layers are formed, resulting in a weaker interaction between the shear layers beneath the cylinder bottom and near the wall. For  $G/D = 0.2$ , however, an increase in  $Re$  does not affect the bottom vortex much due to the wall suppression effect.



**FIG. 7.** Vorticity contours and streamlines (black solid lines) for the flow around an isolated elliptic cylinder of  $AR = 0.4$  for (a)  $Re = 30$  and (b)  $Re = 40$ , and for the flow around an elliptic cylinder of  $AR = 0.4$  for  $Re = 40$  at (c)  $G/D = 0.4$  and (d)  $G/D = 0.2$ .





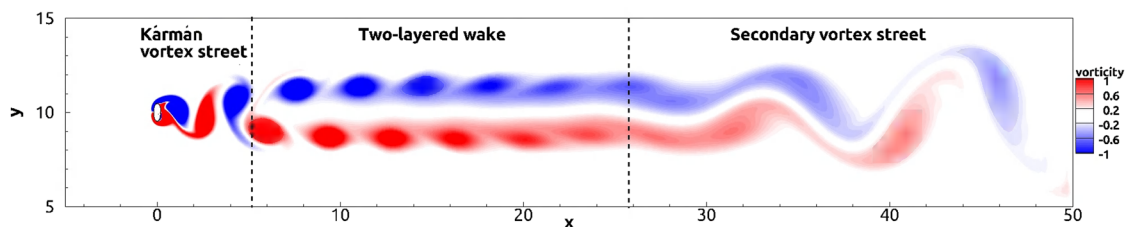
**FIG. 8.** (a) Locations of the vortex center behind the cylinder; (b) the drag ( $C_D$ ) and lift ( $C_L$ ) coefficient for  $Re$  from 30 to 70 and for  $G/D = 0.2$  and  $0.4$ ; and (c) and (d) show the pressure ( $P_x$ ) and skin friction drag ( $F_x$ ) coefficients, respectively, for  $Re$  from 30 to 70 and for  $G/D = 0.2$  and  $0.4$ .

Figure 8(b) shows  $C_D$  and  $C_L$  against  $Re$  in the steady flow regime, i.e., for  $Re \in [30, 100]$  at  $G/D = 0.2$  and  $0.4$ . For a given  $Re$ ,  $C_D$  and  $C_L$  are larger for  $G/D = 0.2$  than for  $G/D = 0.4$ . For a given gap ratio,  $C_D$  and  $C_L$  decrease almost linearly as  $Re$  increases in the log-log scale. This is in qualitative agreement with the results observed previously by Rao *et al.*<sup>43,44</sup> (for the steady flow regime, i.e., no vortex shedding) for a fixed and a rotating circular cylinder near a moving wall for  $G/D$  ranging from 0.05 to 4. Figures 8(c) and 8(d) show the drag force due to the pressure ( $P_x$ ) and due to the skin friction ( $F_x$ ) against  $Re$  for  $G/D = 0.2$  and  $0.4$ , respectively. It appears that  $G/D$  has a weaker effect on  $F_x$  than on  $P_x$ , implying that the  $G/D$  affects the cylinder friction less than the pressure distribution around the cylinder as previously demonstrated by Sumer and Fredsøe<sup>25</sup> for a circular cylinder.

## B. Unsteady state

### 1. Wake patterns

Figure 9 shows the vorticity contours of the flow around an isolated elliptic cylinder with  $AR = 0.4$  for  $Re = 130$ . The three different wake structures (separated by vertical dashed lines) can be classified into three different flow regimes:<sup>11,28</sup> (i) the near wake where clockwise and anti-clockwise vortices are alternately shed from the upper and lower parts of the cylinder, forming the Kármán vortex street; (ii) further downstream, the Kármán vortex street breaks down and develops into a two-layered wake,<sup>6,7,28</sup> and (iii) the far wake where the hydrodynamic instability of the two-layered wake<sup>8,17</sup> leads to a secondary vortex street characterized by larger scales and lower frequencies than the Kármán vortex street.



**FIG. 9.** Vorticity contours for the flow around an isolated elliptic cylinder of  $AR = 0.4$  with  $Re = 130$ .

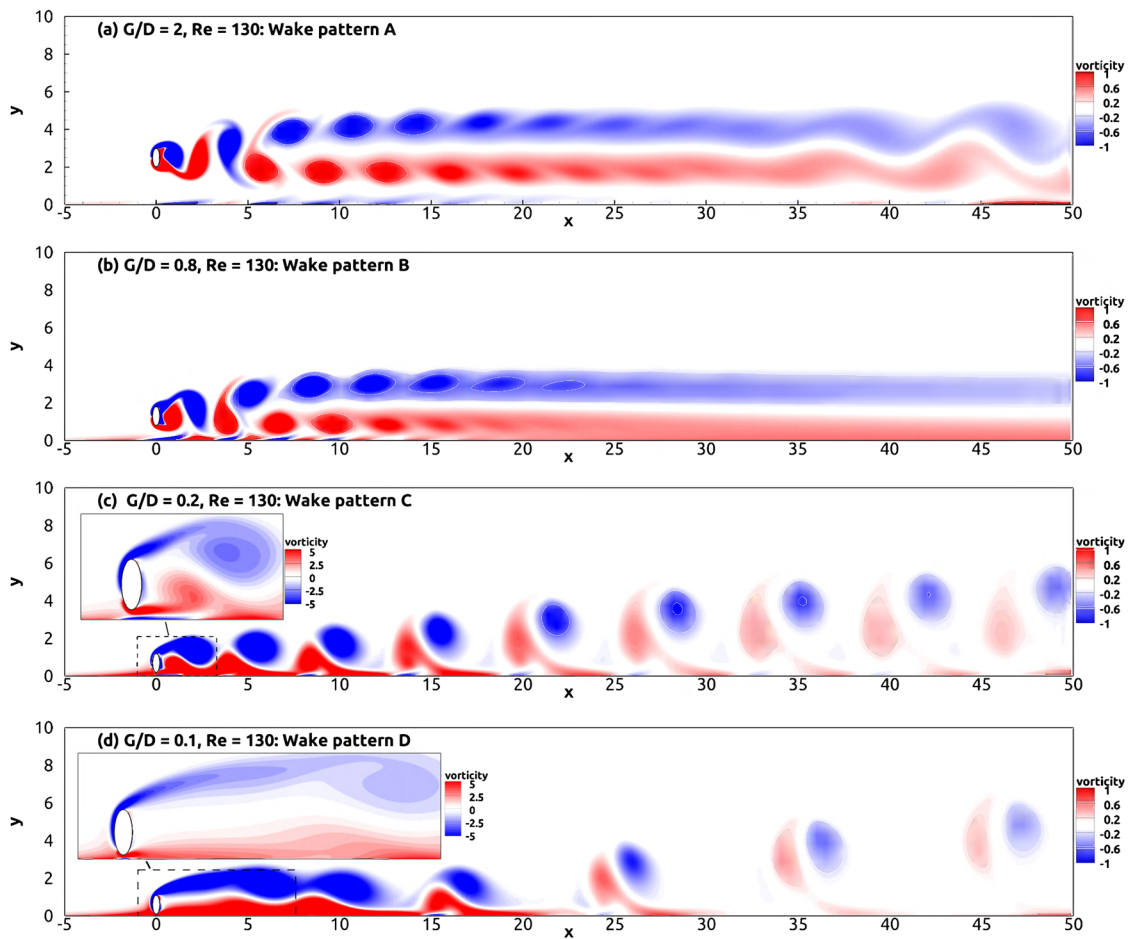


FIG. 10. Instantaneous vorticity contours for the flow around an elliptic cylinder of  $AR = 0.4$  near a moving wall with  $Re = 130$  and  $G/D = 2, 0.8, 0.2,$  and  $0.1$ .

Figure 10 shows the instantaneous vorticity contours for the flow around an elliptic cylinder near a moving wall for  $Re = 130$  and for  $G/D = 2, 0.8, 0.2,$  and  $0.1$ . For  $G/D = 2$  [Fig. 10(a)], the wake structure is composed of the Kármán vortex street, the two-layered wake, and the secondary vortex street. This flow structure is qualitatively similar to that of an isolated elliptic cylinder (Fig. 9). Moreover, it is worth noting that the onset location of the two-layered wake is nearly the same (this will be further discussed in Sec. V B 3), while the secondary vortex occurs farther downstream for  $G/D = 2$  than for the isolated cylinder. The bottom wall shear layer is a result of the vortex (with positive vorticity) shed from the cylinder bottom, a region with negative vorticity occurs between the vortex and the wall. This result is valid for a vortex in the vicinity of a wall as first predicted by Peace and Riley,<sup>45</sup> observed experimentally by Walker *et al.*<sup>46</sup> and Allen and Chong,<sup>47</sup> and shown by Ovando *et al.*<sup>48</sup> and Zhu *et al.*<sup>49</sup> using numerical simulations. This flow is denoted as wake pattern A. Figure 11 shows the amplitude  $v_a$  of the vertical velocity fluctuation along the downstream cylinder centerline for the isolated cylinder and for  $G/D = 2$  and  $0.8$ . In the near-wake region,  $v_a$  decreases downstream [which is consistent with the decay

of the Kármán vortex street and the transition to the two-layered wake where a calm region is formed between the two vortex layers; see Figs. 9, 10(a), and 10(b)]. Then,  $v_a$  grows farther downstream for the isolated cylinder and for  $G/D = 2$ , which coincides with the transition from the two-layered wake to the secondary vortex street

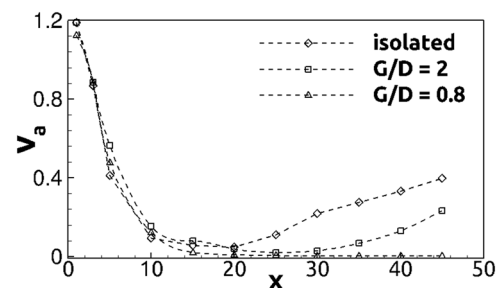


FIG. 11. Amplitude of the vertical velocity fluctuation along the wake centerline for the isolated cylinder and for  $G/D = 0.8$  and  $2$  at  $Re = 130$ .

[see Figs. 9 and 10(a)]. Furthermore, Fig. 11 shows that the presence of the moving wall leads to a significant reduction in  $v_a$  in the far-wake region, consistent with the delayed onset of the secondary vortex street for  $G/D = 2$ ; the secondary vortex street appears farther downstream for  $G/D = 2$  [Fig. 10(a)] than for the isolated cylinder (Fig. 9).

As  $G/D$  decreases to 0.8 [Fig. 10(b)], the secondary vortex street disappears in the far wake region, which is present for  $G/D = 2$  [Fig. 10(a)] and for the isolated cylinder (Fig. 9). This is consistent with the observation that  $v_a$  remains almost zero in the far wake region (Fig. 11), i.e., the vertical fluctuations are further suppressed as the wall is approached. Thus, the wake structure here is composed of the Kármán vortex street and the two-layered wake; this flow is denoted as wake pattern B. Here, the onset location of the two-layered wake for  $G/D = 0.8$  is closer to the cylinder than for  $G/D = 2$ . This will be further discussed and quantified in Sec. V B 3.

As  $G/D$  decreases to 0.2 [Fig. 10(c)], the lower vortex (behind the bottom of the cylinder) is shed immediately following the upper one (behind the top of the cylinder), forming a vortex pair moving downstream and deflecting away from the wall. This pair-wise vortex shedding destroys the geometric arrangement of the vortices required for the transition to the two-layered wake. Thus, the Kármán vortex street and the two-layered wake break down simultaneously; this flow is denoted as wake pattern C.

For  $G/D = 0.1$  [Fig. 10(d)], the upper shear layer (behind the top of the cylinder) becomes more elongated than for  $G/D = 0.2$  and

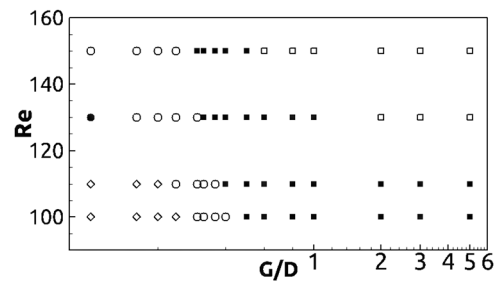


FIG. 12. Distribution of wake patterns, i.e., wake pattern A (□), wake pattern B (■), wake pattern C (○), wake pattern D (●), and the steady state (◇) within  $(G/D, Re)$ -space.

rolls down at a downstream location of  $x \approx 5$ . The shear layer near the wall rolls up when meeting the rolled-down shear layer at  $x \approx 15$ , forming a new vortex pair moving downstream and deflecting away from the wall. This behavior is qualitatively similar to that observed for  $G/D = 0.2$ , except for the existence of a quasi-steady near-wake region ( $x < 5$ ), where the drag and lift coefficients are almost constant, as will be discussed in Sec. V B 2; this flow is denoted as wake pattern D.

Figure 12 shows the distribution of the wake patterns A, B, C, and D as well as the steady state flow (i.e., no vortex shedding occurs)

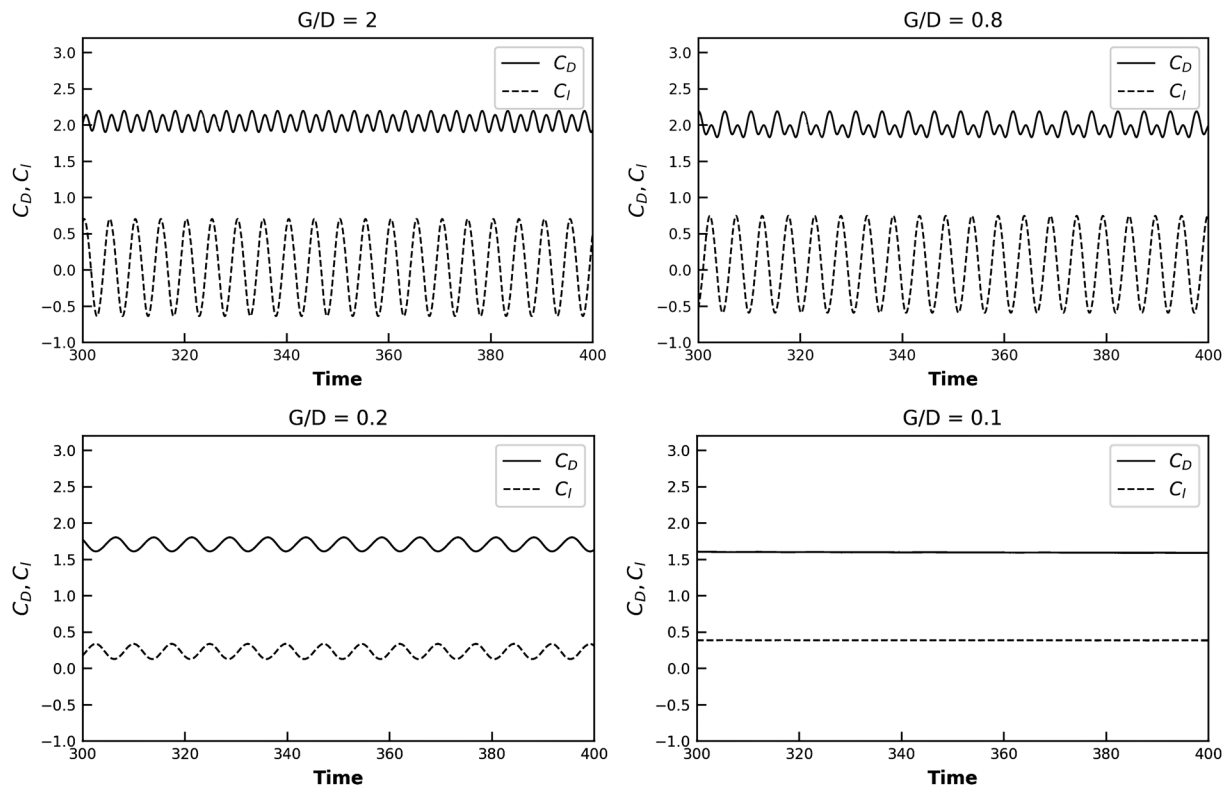


FIG. 13. Time history of  $C_D$  and  $C_l$  for the flow around an elliptic cylinder of  $AR = 0.4$  near a moving wall with  $Re = 130$  and  $G/D = 2, 0.8, 0.2,$  and  $0.1$ .

in the  $(G/D, Re)$ -space. Wake pattern  $D$  only exists at  $G/D = 0.1$  for  $Re = 130$ . For  $Re \leq 110$ , wake pattern  $A$  does not exist (i.e., the secondary vortex street does not appear), and the steady state flow appears only at small values of  $G/D$  and  $Re$ . Overall, it appears that as  $G/D$  decreases (for a given  $Re$ ), the flow undergoes a transition sequence from wake pattern  $A \rightarrow$  wake pattern  $B \rightarrow$  wake pattern  $C$ . Moreover, as  $Re$  increases (for a given  $G/D$ ), the critical gap ratio  $G/D_c$  for the transition between two wake patterns (except wake pattern  $D$ ) decreases. This critical gap ratio  $G/D_c$  denotes a threshold value where one wake pattern exists and below which another wake pattern appears. For example, the transition between wake patterns  $B$  and  $C$  occurs for  $G/D \in [0.36, 0.4]$  (where  $G/D_c = 0.38 \pm 0.02$ ) for  $Re = 110$  and for  $G/D \in [0.3, 0.32]$  (where  $G/D_c = 0.31 \pm 0.01$ ) for  $Re = 130$ . This might be explained by that an increase in  $Re$  leads to an enhanced growth of the secondary instability (i.e., the transition of wake patterns  $B$  to  $A$ ) as well as the vortex shedding behind the bottom of the cylinder (i.e., the transition from the steady state flow to wake pattern  $C$ ). Conversely, a decrease in  $G/D$  suppresses the growth of  $v_a$  (i.e., the secondary instability) in the far-wake region (Fig. 11) and the Kármán vortex shedding. Therefore, a smaller  $G/D$  is required for a higher  $Re$  to maintain the same wake pattern.

### 2. Hydrodynamic forces

Figure 13 shows the time history of the drag coefficient  $C_D$  and the lift coefficient  $C_l$  for the flow around an elliptic cylinder near a moving wall for  $Re = 130$  at  $G/D = 2, 0.8, 0.2$ , and  $0.1$ , i.e., corresponding to the flow shown in Fig. 10. For both  $G/D = 2$  and  $G/D = 0.8$ , it is observed that every second crest value of  $C_D$  is larger than the crest values in between; this effect is strongest for  $G/D = 0.8$ . The smaller crest values are caused by the vortex shed from the bottom part of the cylinder, while the larger crest values are caused by the vortex shed from the top of the cylinder.<sup>24,50</sup> It is observed that the lift coefficient  $C_l$  oscillates with half the frequency of  $C_D$  both for  $G/D = 2$  and  $G/D = 0.8$  since two vortices with opposite sign are shed from the top and bottom of the cylinder within each oscillation period and  $C_D$  is not sensitive to the sign of the vortex.<sup>51</sup> For  $G/D = 0.2$ , the upper and lower vortices are not shed alternately; the lower vortex is shed and follows the upper vortex immediately, forming a vortex pair moving downstream [as previously shown in Fig. 10(c)]. Consequently, the small crest caused by the alternately shedding lower vortex [see, e.g., Figs. 10(b) and 13 for  $G/D = 0.8$ ] disappears, resulting in a constant crest value of  $C_D$  and the same oscillating frequency but with different phases for  $C_D$  and  $C_l$ . A similar explanation was also found by Huang and Sung<sup>24</sup> for the flow around a circular cylinder near a moving wall with  $G/D = 0.2$  and  $Re = 300$ . As  $G/D$  decreases further to  $0.1$ , the oscillations of  $C_D$  and  $C_l$  vanish since the vortex shedding near the cylinder is suppressed as shown in Fig. 10(d).

Figure 14(a) shows the time-averaged drag coefficient ( $\bar{C}_D$ ), the time-averaged drag coefficients due to the pressure ( $P_x$ ) and due to the skin friction ( $F_x$ ) against  $G/D$  for  $Re = 150$ . Here,  $\bar{C}_D = P_x + F_x$ . The value of  $\bar{C}_D$  increases gradually for  $G/D \in [0.1, 1.4]$ , except for a sudden drop at  $G/D \in [0.24, 0.3]$ , which will be further explained below. For  $G/D$  larger than  $1.4$ ,  $\bar{C}_D$  remains nearly constant. A similar behavior is observed for  $P_x$ , while  $F_x$  is hardly affected by  $G/D$  at all. The overall increase in  $\bar{C}_D$  as  $G/D$  increases is mainly due to the time-averaged pressure difference over the cylinder, which is closely

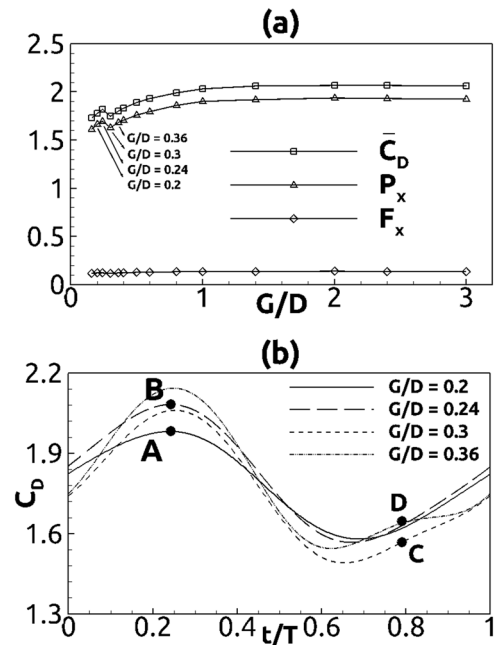


FIG. 14. (a) Variations of the time-averaged drag coefficient ( $\bar{C}_D$ ), viscous ( $F_x$ ), and pressure ( $P_x$ ) drag coefficients at various  $G/D$  for  $Re = 150$ . (b) Time history of the  $C_D$  for  $Re = 150$  and for  $G/D = 0.2, 0.24, 0.3$ , and  $0.36$ . Here,  $T$  is the vortex shedding period, which is different for different  $G/D$ .

related to the growth of the vortex attached to the backside of the cylinder, as shown in Fig. 15; a stronger attached vortex draws in fluid more rapidly from the base region behind the cylinder during its growth, leading to a smaller pressure behind the cylinder and thus a larger pressure difference over the cylinder, leading to larger values of  $P_x$  and thus of  $\bar{C}_D$ .

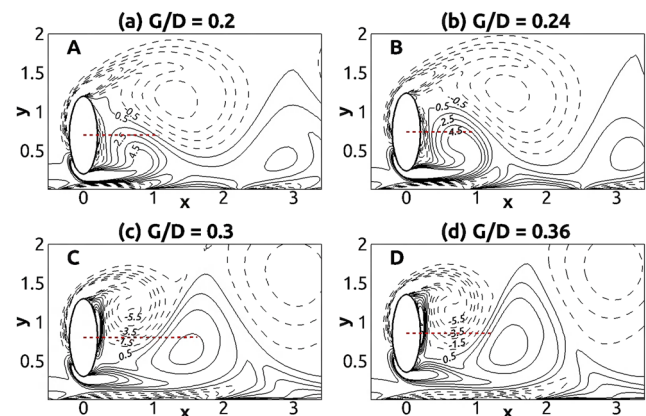


FIG. 15. Vorticity contours for the flow around an elliptic cylinder near a moving wall with  $G/D = 0.2, 0.24, 0.3$ , and  $0.36$  at instants  $A, B, C$ , and  $D$ , respectively, marked in Fig. 14; for contours with values from  $-5.5$  to  $5.5$ , the difference in value between two adjacent contour lines is 1. Dashed and solid lines indicate the negative and positive values, respectively.

Here, the increase in  $\bar{C}_D$  for  $G/D \in [0.2, 0.24]$  and  $G/D \in [0.3, 0.36]$  observed in Fig. 14(a) is investigated; the decay of  $\bar{C}_D$  for  $G/D \in [0.24, 0.3]$  will be discussed in the paragraph below. The time-history of  $C_D$  at  $G/D = 0.2, 0.24, 0.3,$  and  $0.36$  for  $Re = 150$  during one dimensionless vortex shedding cycle is shown in Fig. 14(b). Here, the largest value of  $C_D$  is smaller for  $G/D = 0.2$  than for  $G/D = 0.24$  (marked as A and B, respectively). This coincides with the occurrence of the lower vortex behind the bottom of the cylinder shown in Figs. 15(a) and 15(b), which shows that the lower vortex becomes stronger (i.e., the vorticity increases) as  $G/D$  increases from 0.2 to 0.24. This is because an increase in  $G/D$  weakens the effect of the bottom-wall shear layer on the vortex shedding, thus contributing to the formation of the stronger lower vortex,<sup>27</sup> i.e., the wall suppression effect on the lower vortex shedding becomes weaker. Thus, an increase in  $G/D$  enhances the dimensionless vortex shedding frequency here represented by the Strouhal number  $St$  as shown in Fig. 16(a) for the moving wall (the case of applying the slip wall condition will be discussed below). Figure 14(b) shows that  $C_D$  is smaller for  $G/D = 0.3$  than for  $G/D = 0.36$  at the instants C and D, coinciding with the occurrence of the upper vortex, which is weaker for  $G/D = 0.3$  than for  $G/D = 0.36$  as shown in Figs. 15(c) and 15(d), respectively. This is because the circulation generated at the front of the cylinder is injected into the upper vortex over the cylinder top with lower frequency for  $G/D = 0.3$  than for  $G/D = 0.36$  [consistent with the variation of  $St$  as shown in Fig. 16(a) for a moving wall]. This behavior can be quantified by the cycle-averaged circulation  $\bar{\Gamma}_{top} (= -\frac{1}{T} \int_0^T (\int_{G/D+1}^2 u\omega_z dy) dt)$  and  $\bar{\Gamma}_{gap} (= \frac{1}{T} \int_0^T (\int_0^{G/D} u\omega_z dy) dt)$  (will be discussed below), which represent the rate of the circulation generated at the front of the cylinder injected into the upper and lower vortices shed from the cylinder, respectively. Figure 16(b) shows a smaller  $\bar{\Gamma}_{top}$  for  $G/D = 0.3$  than for  $G/D = 0.36$ , leading to a weaker upper vortex for  $G/D = 0.3$  than for  $G/D = 0.36$ , thus resulting in a smaller  $C_D$  for  $G/D = 0.3$  than for  $G/D = 0.36$ . This behavior is also observed as  $G/D$  increases from 0.2 to 0.24 [Fig. 16(b)], which is consistent with a slightly larger  $C_D$  for  $G/D = 0.24$  than for  $G/D = 0.2$  during the growth phases of the upper vortex (i.e., at instants C and D) shown in Fig. 14(b). Overall, it appears that for  $G/D \in [0.2, 0.24]$  and  $G/D \in [0.3, 0.36]$  an increase in  $G/D$  weakens the wall suppression effect on the vortex shedding behind the cylinder, thus forming a stronger lower vortex behind the cylinder, while the circulation is injected over the top of the cylinder with higher frequency, contributing to a stronger upper vortex.

Now, the sudden drop of  $\bar{C}_D$  for  $G/D \in [0.24, 0.3]$  observed in Fig. 14(a) is discussed. As shown in Fig. 14(b), the value of  $C_D$  is smaller for  $G/D = 0.3$  than for  $G/D = 0.24$  during the entire

shedding cycle. This implies that both the upper and lower vortices are weaker for  $G/D = 0.3$  than for  $G/D = 0.24$ . The formation of the weaker upper and lower vortices for  $G/D = 0.3$  relative to  $G/D = 0.24$  is consistent with the decrease in  $\bar{\Gamma}_{top}$  and  $\bar{\Gamma}_{gap}$  as  $G/D$  increases from 0.24 to 0.3 as shown in Fig. 16(b). It should be noted that the vortex shedding frequency ( $\frac{1}{T}$ ) is almost the same for  $G/D = 0.24$  and 0.3 (which will be further explained in the following paragraph) shown in Fig. 16(b). Hence, the decrease in both  $\bar{\Gamma}_{top}$  and  $\bar{\Gamma}_{gap}$  is determined by the total circulation convecting into the vortices from the top of the cylinder [ $\Gamma_{top} = -\int_0^T (\int_{G/D+1}^2 u\omega_z dy) dt$ ] and through the gap [ $\Gamma_{gap} = \int_0^T (\int_0^{G/D} u\omega_z dy) dt$ ] during one vortex shedding cycle. The decrease in  $\Gamma_{top}$  as  $G/D$  increases from 0.24 to 0.3 is due to less fluid moving upward along the cylinder since the front stagnation point moves upward along the cylinder as  $G/D$  increases, as depicted in Figs. 7(c) and 7(d); the decrease in  $\Gamma_{gap}$  is due to the decrease in the gap velocity as  $G/D$  increases. However, the wall suppression effect is weaker for  $G/D = 0.3$  than for  $G/D = 0.24$ , which (as an isolated effect) would lead to an increase in  $\bar{C}_D$  from  $G/D = 0.24$  to  $G/D = 0.3$ . It appears that for  $G/D \in [0.24, 0.3]$ , the total vortex strength (i.e., from the upper and lower vortices) is stronger affected by the circulation injection rate than by the wall suppression effect. This is in contrast to the case of  $G/D \in [0.2, 0.24]$ , where  $\bar{\Gamma}_{gap}$  decreases, while  $\bar{\Gamma}_{top}$  increases, resulting in that  $\bar{C}_D$  increases, indicating that the lower vortex strength here is stronger affected by the wall suppression than by the circulation generated at the front of the cylinder. Moreover, it is worth noting that  $\bar{\Gamma}_{gap} (= \Gamma_{gap}/T)$  also keeps decreasing as  $G/D$  increases, which is different from  $\bar{\Gamma}_{top}$  and  $\bar{C}_D$ , as shown in Figs. 16(b) and 14(a), respectively. It appears that the decrease in  $T$  induced by increasing  $G/D$  does not compensate the simultaneous decrease in  $\Gamma_{gap}$  due to the decrease in flow velocity in the gap caused by increasing  $G/D$ .

Now, the nearly constant value of  $St$  for  $G/D \in [0.24, 0.3]$  for  $Re = 150$  [Fig. 16(a), the moving wall where the no-slip conditions  $u = 1$  and  $v = 0$  are imposed] is discussed. For a given  $Re$ , the vortex shedding frequency is mainly affected by the wall suppression effect and the bottom-wall shear layer. The effect of these shear layers can be eliminated by conducting simulations with a slip condition ( $\frac{\partial u}{\partial y} = 0, v = 0$ ) imposed on the bottom wall. At large gap ratios, e.g., for  $G/D > 0.3$  [Fig. 16(a)],  $St$  is almost equal for the two boundary conditions because the shedding vortices are weakly affected by the bottom-wall shear layers. Here,  $St$  increases as  $G/D$  increases due to the weakening of the wall suppression effect. For  $G/D \in [0.2, 0.24]$ , the vortex suppression effect is larger than for  $G/D > 0.3$ , but in this gap ratio range, the bottom-wall shear layers cause the vortex shed from the cylinder bottom to roll up such that it is located closer to the vortex shed from the cylinder top. This results in an

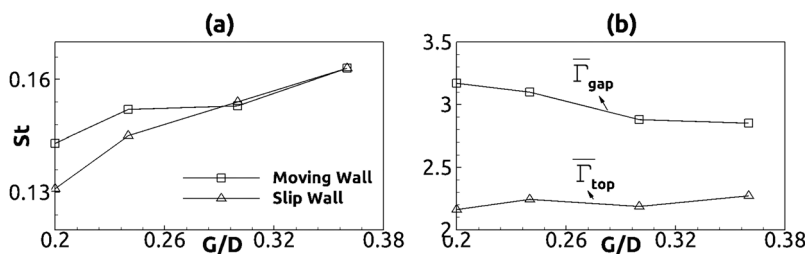


FIG. 16. (a) The Strouhal number  $St$  and (b) the injection rate  $\bar{\Gamma}_{top}$  of the circulation into the upper vortex over the top of the cylinder and the injection rate  $\bar{\Gamma}_{gap}$  of the circulation into the lower vortex through the gap for  $Re = 150$  with  $G/D = 0.2, 0.24, 0.3,$  and  $0.36$ .

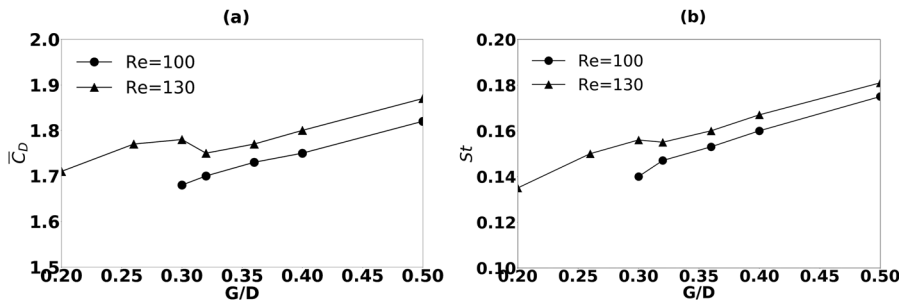


FIG. 17. (a) The time-averaged drag coefficient  $\bar{C}_D$  and (b) the Strouhal number  $St$  for the flow around an elliptic cylinder near a moving wall for  $Re = 100$  and  $130$  with  $G/D$  from  $0.2$  to  $0.5$ .

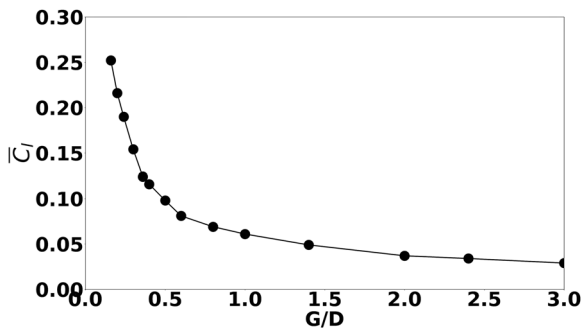


FIG. 18. The mean lift coefficient  $\bar{C}_l$  against  $G/D$  for  $Re = 150$ .

enhancement of the vortex shedding frequency ( $St$ ) for  $G/D \in [0.2, 0.24]$ , which compensates the decrease in  $St$  induced by the strengthening of the wall suppression effect (as  $G/D$  decreases from  $0.3$  to  $0.24$ ), thus resulting in the nearly equal  $St$  for  $G/D \in [0.24, 0.3]$ . Moreover, for  $G/D \in [0.2, 0.24]$ ,  $St$  increases as  $G/D$  increases but is larger than for the case of applying the slip condition, as shown in Fig. 16(a).

Figure 17(a) shows the time-averaged drag coefficient  $\bar{C}_D$  (a) and the Strouhal number  $St$  (b) for  $Re = 100$  and  $130$ . For  $Re = 130$ ,  $\bar{C}_D$  exhibits a qualitatively similar behavior as for  $Re = 150$  [shown in Fig. 14(a)], showing an overall increase in  $\bar{C}_D$  as  $G/D$  increases from  $0.2$  to  $0.3$  with a sudden drop for  $G/D \in [0.3, 0.32]$ . However, the sudden drop of  $\bar{C}_D$  does not occur for  $Re = 100$ . This is because here the bottom-wall shear layer becomes weaker, thus reducing its effect on the vortex shedding frequency at small  $G/D$ , i.e., as  $G/D$  increases the vortex shedding frequency increases smoothly as shown in Fig. 17(b) without a nearly constant region similar to that for  $Re = 130$ . Hence,

the circulation is injected into the vortex with higher frequency as  $G/D$  increases, contributing to a stronger vortex shedding, i.e., a smooth growth of  $\bar{C}_D$ .

Figure 18 shows the time-averaged lift coefficient ( $\bar{C}_l$ ) against  $G/D$  for  $Re = 150$ . The non-zero  $\bar{C}_l$  is caused by the asymmetric flow distribution around the stream-wise centerline of the cylinder due to the presence of the moving wall. As  $G/D$  increases, the flow tends to be less asymmetric, leading to a decrease in  $\bar{C}_l$ . A qualitatively similar behavior was also found for the flow around a circular cylinder near a moving wall for  $Re < 500$ .<sup>24,27,43</sup>

### 3. The onset location of the two-layered wake

As previously proposed by Jiang and Cheng,<sup>11</sup> the onset location of the two-layered wake behind the isolated elliptic cylinder (for  $AR = 0.4$  and for  $Re = 130$ ) can be identified by the location of the positive and negative local maxima of the time-averaged vertical velocity contours [i.e., the vertical dashed line in Fig. 19(a)]. A snapshot of the instantaneous vorticity contours is shown in Fig. 19(b) depicting the Kármán vortex and the two-layered wake farther downstream. Figure 20 shows the time-averaged vertical velocity contours (left column) and the instantaneous vorticity contours (right column) for  $Re = 130$  at  $G/D = 2$  and  $0.8$ . Here, the distribution of the time-averaged velocity becomes asymmetric about the horizontal centerline of the cylinder; the positive local maximum is slightly farther away from the cylinder than the negative maximum. Thus, the transition to the two-layered wake occurs farther downstream for the upper part than for the lower part of the cylinder. This is because the lower vortex behind the cylinder is weaker than the upper vortex due to the wall suppression effect, and thus, the upper vortex induces a stronger vorticity convection within the lower vortex.<sup>6,7</sup> Consequently, the lower vortex distorts and rotates to align with the stream-wise direction at a location closer to the cylinder than the horizontal upper vortex. Here, the negative maximum is

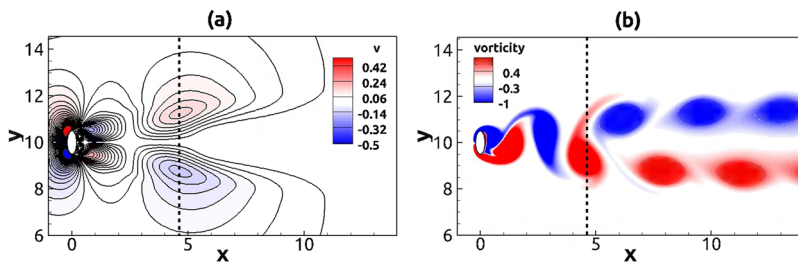
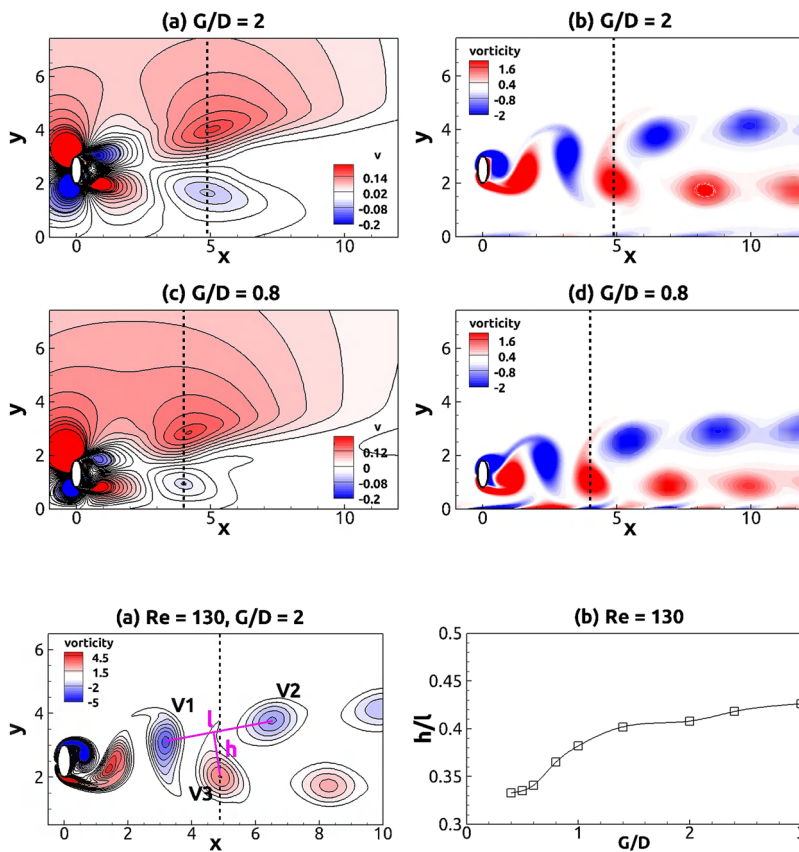


FIG. 19. (a) Time-averaged vertical velocity field and (b) instantaneous vorticity contours for the flow around an isolated cylinder for  $Re = 130$ . The black dashed line denotes the transition location for the two-layered wake.



**FIG. 20.** Time-averaged vertical velocity field (left column) and instantaneous vorticity contours (right column) for the flow around an elliptic cylinder near a moving wall for  $Re = 130$  with  $G/D = 2$  and  $0.8$ .

**FIG. 21.** (a) Definition of the spacing ratio  $h/l$  of the Kármán vortices, where  $l$  denotes the distance between two same sign vortices ( $V1$  and  $V2$ ), while  $h$  represents the distance between the positive vortex ( $V3$ ) and the line connecting  $V1$  and  $V2$ . (b) Variations of the threshold value of the spacing ratio  $h/l$  against  $G/D$  for  $Re = 130$ .

used to identify the onset location of the two-layered flow for  $G/D = 2$  and  $0.8$  [Figs. 20(a) and 20(c), respectively]. As  $G/D$  decreases from 2 to 0.8, the distance ( $x_{loc}$ ) between the onset location of the two-layered wake and the cylinder center decreases. This behavior can be further explained by the spacing ratio  $h/l$  of the Kármán vortices<sup>6,7</sup> [Fig. 21(a)], where  $l$  denotes the distance between two same-sign (here negative) vortices ( $V1$  and  $V2$ ), while  $h$  represents the distance between the vortex ( $V3$ ) with opposite sign (here positive) and the line connecting  $V1$  and  $V2$ . This spacing ratio  $h/l$  increases as the Kármán vortices move downstream and then reaches a threshold value at  $x_{loc}$ , where the transition of the two-layered wake occurs.

The threshold value of  $h/l$  is here determined by the center of the  $V3$  vortex being located at the dashed line [determined by the time-averaged vertical velocity, Fig. 20(a)]. Here, the threshold values are 0.453, 0.45, and 0.449 for the isolated elliptic cylinder with  $AR = 0.4$  and  $Re = 100, 130,$  and  $150$ , respectively. This is in qualitative agreement with the results obtained by Durgin and Karlsson<sup>6</sup> and Karasudani and Funakoshi<sup>7</sup> for an isolated circular cylinder, reporting the threshold values in the range of 0.45–0.5 for  $Re$  ranging from 80 to 150. It appears that the threshold value does not vary much with  $AR$  and  $Re$  in the absence of the wall; the threshold value is dominated by the wall. The wall suppression effect leads to the  $V1$  and  $V2$  vortices being stronger than the  $V3$  vortex, thus causing a stronger vorticity convection within the  $V3$  vortex than that

for the isolated cylinder where these three vortices are of almost equal strength.<sup>6</sup> Consequently, the  $V3$  vortex distorts and rotates closer to the cylinder as  $G/D$  decreases (i.e., as the wall suppression becomes stronger), forming the two-layered wake, i.e.,  $x_{loc}$  decreases as  $G/D$  decreases, as shown in Fig. 22. This coincides with the behavior for the threshold value of  $h/l$ , which decreases with decreasing  $G/D$ , as shown in Fig. 21(b) for  $Re = 130$ . In contrast,  $x_{loc}$  increases as  $G/D$  decreases from 0.6 to 0.5 for  $Re = 100$  and from

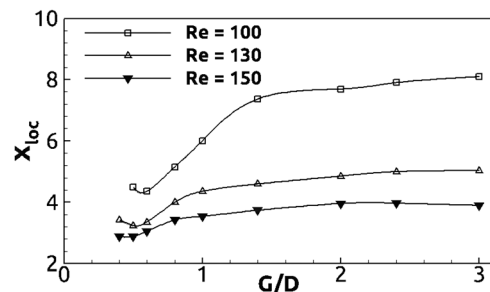


**FIG. 22.** The distance ( $x_{loc}$ ) between the onset location of the two-layered wake and the cylinder center for  $G/D$  from 3 to 0.2 and for  $Re = 100, 130,$  and  $150$ .

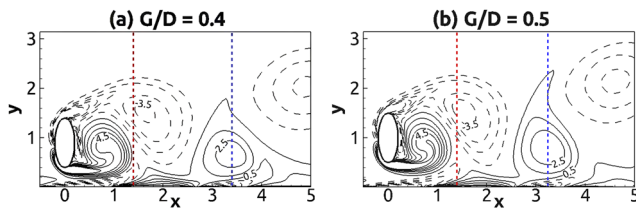


**FIG. 23.** The vorticity contours for the flow around an elliptic cylinder near a moving wall for  $Re = 130$  with  $G/D = 0.4$  and  $0.5$ ; for contours with values from  $-5.5$  to  $5.5$ , the difference in value between two adjacent contour lines is  $1$ . Black dashed and solid lines indicate the negative and positive values, respectively, while the red and blue dashed lines denote a reference line at  $x = 1.4$  and the onset location of the two-layered wake, respectively.

$0.5$  to  $0.4$  for  $Re = 130$ . It appears that an increase in the low velocity in the gap with decreasing  $G/D$  leads to the lower shear layer beneath the cylinder rolling up slightly farther downstream for  $G/D = 0.4$  [Fig. 23(a)] than for  $G/D = 0.5$  [Fig. 23(b)], thus resulting in a larger  $x_{loc}$ .

Thompson *et al.*<sup>28</sup> investigated the effect of  $Re$  on  $x_{loc}$  for the flow around an isolated elliptic cylinder for  $AR \in [0.25, 1]$  and found that  $x_{loc}$  decreases as  $Re$  increases from  $100$  to  $150$ . This is because an increase in  $Re$  leads to a stronger increase in  $h/l$  downstream, resulting in the threshold value of  $h/l$  being achieved closer to the cylinder. This behavior is qualitatively similar to that observed in Fig. 22 for a given  $G/D$ . Moreover,  $x_{loc}$  is less sensitive to  $G/D$  when  $G/D > 1.4$  for  $Re = 100$  and  $G/D > 1$  for  $Re = 130$  and  $150$ . This can be explained by that a decrease in  $Re$  forms a thicker shear layer on the bottom of the cylinder, which starts to interact with the bottom-wall shear layer at a relatively large  $G/D$  for low  $Re$ .<sup>52</sup>

## VI. SUMMARY AND CONCLUSIONS

In this work, the flow over an elliptic cylinder near a moving wall is investigated for Reynolds numbers less than  $150$ . Here, the ratio between the gap (i.e., the distance between the cylinder and the wall) and the length of the semi-major axis of the elliptic cylinder varies from  $0.1$  to  $5$ . This ratio is hereafter denoted as the gap ratio. The resulting Kármán vortex street, the two-layered wake, and the secondary vortex street have been investigated and visualized.

In the steady flow regime, the wake contains two asymmetric counter-rotating recirculation vortices attached to the cylinder. Here, the lower vortex center is located closer to the cylinder than the upper vortex center. This difference increases as the gap ratio decreases (for a given Reynolds number) due to the stronger wall suppression effect on the lower vortex for lower gap ratios. As the Reynolds number increases (for a given gap ratio), this difference decreases since thinner shear layers are formed, resulting in a weaker interaction between the shear layers beneath the cylinder bottom and above the wall. Moreover, as the gap ratio decreases (for a given Reynolds number), the time-averaged drag coefficient decreases, while the time-averaged lift coefficient increases; as the Reynolds number increases (for a given gap ratio), the drag and lift coefficients decrease almost linearly in the log–log scale.

In the unsteady flow regime, four different wake patterns have been classified: (i) at relatively large gap ratios, the flow, which is denoted as wake pattern A, contains the Kármán vortex street, the two-layered wake, and the secondary vortex street; (ii) a decrease in the gap ratio leads to the suppression of the vertical fluctuations in the far-wake region, resulting in the disappearance of the secondary vortex street; this represents wake pattern B; (iii) a further decrease in the gap ratio leads to the break-down of the Kármán vortex, resulting in a pair-wise vortex shedding (denoted as wake pattern C); or (iv) forming a quasi-steady near-wake region (with constant lift and drag coefficients) and a pair-wise vortex shedding farther downstream, which is denoted as wake pattern D. Moreover, an increase in the Reynolds number (for a given gap ratio) enhances the vortex shedding behind the cylinder, thus triggering the transition between two different wake patterns. Therefore, a smaller gap ratio is required for a higher Reynolds number to maintain the same wake pattern, i.e., a smaller critical gap ratio is required for the transition between two different wake patterns (except for wake pattern D).

The time-averaged drag coefficient increases gradually as the gap ratio increases (for a given Reynolds number) due to the decay of the wall suppression effect. A sudden drop of the time-averaged drag coefficient is observed as the gap ratio increases from  $0.3$  to  $0.32$  and from  $0.24$  to  $0.3$  for Reynolds numbers of  $130$  and  $150$ , respectively, where the vortex shedding frequency remains nearly constant. It appears that the vortex strength here is determined by the total circulation injected into the wake from the top and the bottom of the cylinder. This total circulation decreases as the gap ratio increases due to less fluid moving upward along the cylinder and a decrease in the flow velocity. Consequently, weaker upper and lower vortices are formed for larger gap ratios, resulting in a sudden drop of the time-averaged drag coefficient. Moreover, the time-averaged lift coefficient increases as the gap ratio decreases (for a given Reynolds number) due to more asymmetric flow distribution around the cylinder.

A stronger wall suppression effect for smaller gap ratios leads to the upper vortex being stronger than the lower vortices, thus enhancing the convection of the vorticity within the lower vortex. Consequently, the lower vortex distorts and rotates to align with the stream-wise direction at a location closer to the cylinder than the horizontal upper vortex, showing that the onset location of the two-layered wake moves closer to the cylinder as the gap ratio decreases (for a given Reynolds number).

Overall, the present work gives some insight into the physical process of transitional movements of bluff bodies near a stationary plane wall (including the far-wake dynamics), which is relevant for engineering and geophysical applications, such as an AUV moving over the seabed. In future studies, the effects of the aspect ratio and the angle of attack, as well as the effect of turbulence on this physical process (i.e., on wake patterns and drag and lift coefficients) should be addressed.

## ACKNOWLEDGMENTS

We gratefully acknowledge the support for this research from the Department of Marine Technology, Norwegian University of Science and Technology and the China Scholarship Council (Grant No. 201506680058).



## DATA AVAILABILITY

The data that support the findings of this study are available from the corresponding author upon reasonable request.

## REFERENCES

- <sup>1</sup>S. C. R. Dennis and G.-Z. Chang, "Numerical solutions for steady flow past a circular cylinder at Reynolds numbers up to 100," *J. Fluid Mech.* **42**, 471–489 (1970).
- <sup>2</sup>S. Sen, S. Mittal, and G. Biswas, "Steady separated flow past a circular cylinder at low Reynolds numbers," *J. Fluid Mech.* **620**, 89–119 (2009).
- <sup>3</sup>P. Le Gal, A. Nadim, and M. Thompson, "Hysteresis in the forced Stuart–Landau equation: Application to vortex shedding from an oscillating cylinder," *J. Fluids Struct.* **15**, 445–457 (2001).
- <sup>4</sup>B. Kumar and S. Mittal, "Effect of blockage on critical parameters for flow past a circular cylinder," *Int. J. Numer. Methods Fluids* **50**, 987–1001 (2006).
- <sup>5</sup>J. M. Cimbalá, H. M. Nagib, and A. Roshko, "Large structure in the far wakes of two-dimensional bluff bodies," *J. Fluid Mech.* **190**, 265–298 (1988).
- <sup>6</sup>W. W. Durgin and S. K. F. Karlsson, "On the phenomenon of vortex street breakdown," *J. Fluid Mech.* **48**, 507–527 (1971).
- <sup>7</sup>T. Karasudani and M. Funakoshi, "Evolution of a vortex street in the far wake of a cylinder," *Fluid Dyn. Res.* **14**, 331 (1994).
- <sup>8</sup>B. Kumar and S. Mittal, "On the origin of the secondary vortex street," *J. Fluid Mech.* **711**, 641–666 (2012).
- <sup>9</sup>T. Matsui and M. Okude, "Formation of the secondary vortex street in the wake of a circular cylinder," in *Structure of Complex Turbulent Shear Flow* (Springer, 1983), pp. 156–164.
- <sup>10</sup>C. H. K. Williamson and A. Prasad, "Acoustic forcing of oblique wave resonance in the far wake," *J. Fluid Mech.* **256**, 315–341 (1993).
- <sup>11</sup>H. Jiang and L. Cheng, "Transition to the secondary vortex street in the wake of a circular cylinder," *J. Fluid Mech.* **867**, 691–722 (2019).
- <sup>12</sup>M. R. Arif and N. Hasan, "Performance of characteristic numerical boundary conditions for mixed convective flows past a heated square cylinder using a non-Boussinesq approach," *Numer. Heat Transfer, Part A* **76**, 254–280 (2019).
- <sup>13</sup>M. R. Arif and N. Hasan, "Vortex shedding suppression in mixed convective flow past a square cylinder subjected to large-scale heating using a non-Boussinesq model," *Phys. Fluids* **31**, 023602 (2019).
- <sup>14</sup>R. Mittal and S. Balachandar, "Direct numerical simulation of flow past elliptic cylinders," *J. Comput. Phys.* **124**, 351–367 (1996).
- <sup>15</sup>W. A. Khan, J. R. Culham, and M. M. Yovanovich, "Fluid flow around and heat transfer from elliptical cylinders: Analytical approach," *J. Thermophys. Heat Transfer* **19**, 178–185 (2005).
- <sup>16</sup>S. A. Johnson, M. C. Thompson, and K. Hourigan, "Flow past elliptical cylinders at low Reynolds numbers," in *14th Australasian Fluid Mechanics Conference* (Elsevier, Amsterdam, 2001).
- <sup>17</sup>S. A. Johnson, M. C. Thompson, and K. Hourigan, "Predicted low frequency structures in the wake of elliptical cylinders," *Eur. J. Mech. B: Fluids* **23**, 229–239 (2004).
- <sup>18</sup>S. K. Raman, K. Arul Prakash, and S. Vengadesan, "Effect of axis ratio on fluid flow around an elliptic cylinder—A numerical study," *J. Fluids Eng.* **135**, 111201 (2013).
- <sup>19</sup>H. S. Yoon, J. Yin, C. Choi, S. Balachandar, and M. Y. Ha, "Bifurcation of laminar flow around an elliptic cylinder at incidence for low Reynolds numbers," *Prog. Comput. Fluid Dyn., Int. J.* **16**, 163–178 (2016).
- <sup>20</sup>I. Paul, K. A. Prakash, and S. Vengadesan, "Onset of laminar separation and vortex shedding in flow past unconfined elliptic cylinders," *Phys. Fluids* **26**, 023601 (2014).
- <sup>21</sup>R. Subburaj, P. Khandelwal, and S. Vengadesan, "Numerical study of flow past an elliptic cylinder near a free surface," *Phys. Fluids* **30**, 103603 (2018).
- <sup>22</sup>S. Taneda, "Experimental investigation of vortex streets," *J. Phys. Soc. Jpn.* **20**, 1714–1721 (1965).
- <sup>23</sup>M. Zdravkovich, "Observation of vortex shedding behind a towed circular cylinder near a wall," in *Flow Visualization III* (Springer, 1985), pp. 423–427.
- <sup>24</sup>W.-X. Huang and H. J. Sung, "Vortex shedding from a circular cylinder near a moving wall," *J. Fluids Struct.* **23**, 1064–1076 (2007).
- <sup>25</sup>B. M. Sumer and J. Fredsøe, *Hydrodynamics Around Cylindrical Structures* (World Scientific, 2006), Vol. 26.
- <sup>26</sup>P. W. Bearman and D. M. Trueman, "An investigation of the flow around rectangular cylinders," *Aeronaut. Q.* **23**, 229–237 (1972).
- <sup>27</sup>H. Jiang, L. Cheng, S. Draper, and H. An, "Two- and three-dimensional instabilities in the wake of a circular cylinder near a moving wall," *J. Fluid Mech.* **812**, 435–462 (2017).
- <sup>28</sup>M. C. Thompson, A. Radi, A. Rao, J. Sheridan, and K. Hourigan, "Low-Reynolds-number wakes of elliptical cylinders: From the circular cylinder to the normal flat plate," *J. Fluid Mech.* **751**, 570–600 (2014).
- <sup>29</sup>H. A. Van der Vorst, "Bi-CGSTAB: A fast and smoothly converging variant of Bi-CG for the solution of nonsymmetric linear systems," *SIAM J. Sci. Stat. Comput.* **13**, 631–644 (1992).
- <sup>30</sup>N. Peller, A. L. Duc, F. Tremblay, and M. Manhart, "High-order stable interpolations for immersed boundary methods," *Int. J. Numer. Methods Fluids* **52**, 1175–1193 (2006).
- <sup>31</sup>M. Coutanceau and R. Bouard, "Experimental determination of the main features of the viscous flow in the wake of a circular cylinder in uniform translation. Part 1. Steady flow," *J. Fluid Mech.* **79**, 231–256 (1977).
- <sup>32</sup>M. N. Linnick and H. F. Fasel, "A high-order immersed interface method for simulating unsteady incompressible flows on irregular domains," *J. Comput. Phys.* **204**, 157–192 (2005).
- <sup>33</sup>B. Fornberg, "A numerical study of steady viscous flow past a circular cylinder," *J. Fluid Mech.* **98**, 819–855 (1980).
- <sup>34</sup>D. V. Patil and K. N. Lakshmisha, "Finite volume TVD formulation of lattice Boltzmann simulation on unstructured mesh," *J. Comput. Phys.* **228**, 5262–5279 (2009).
- <sup>35</sup>K. Taira and T. Colonius, "The immersed boundary method: A projection approach," *J. Comput. Phys.* **225**, 2118–2137 (2007).
- <sup>36</sup>P. A. Berthelsen and O. M. Faltinsen, "A local directional ghost cell approach for incompressible viscous flow problems with irregular boundaries," *J. Comput. Phys.* **227**, 4354–4397 (2008).
- <sup>37</sup>C. H. K. Williamson, "Oblique and parallel modes of vortex shedding in the wake of a circular cylinder at low Reynolds numbers," *J. Fluid Mech.* **206**, 579–627 (1989).
- <sup>38</sup>D. Calhoun, "A cartesian grid method for solving the two-dimensional streamfunction-vorticity equations in irregular regions," *J. Comput. Phys.* **176**, 231–275 (2002).
- <sup>39</sup>D. Russell and Z. J. Wang, "A cartesian grid method for modeling multiple moving objects in 2D incompressible viscous flow," *J. Comput. Phys.* **191**, 177–205 (2003).
- <sup>40</sup>S. Xu and Z. J. Wang, "An immersed interface method for simulating the interaction of a fluid with moving boundaries," *J. Comput. Phys.* **216**, 454–493 (2006).
- <sup>41</sup>Z. Wang, J. Fan, and K. Cen, "Immersed boundary method for the simulation of 2D viscous flow based on vorticity–velocity formulations," *J. Comput. Phys.* **228**, 1504–1520 (2009).
- <sup>42</sup>C. P. Jackson, "A finite-element study of the onset of vortex shedding in flow past variously shaped bodies," *J. Fluid Mech.* **182**, 23–45 (1987).
- <sup>43</sup>A. Rao, M. C. Thompson, T. Leweke, and K. Hourigan, "The flow past a circular cylinder translating at different heights above a wall," *J. Fluids Struct.* **41**, 9–21 (2013).
- <sup>44</sup>A. Rao, M. C. Thompson, T. Leweke, and K. Hourigan, "Flow past a rotating cylinder translating at different gap heights along a wall," *J. Fluids Struct.* **57**, 314–330 (2015).
- <sup>45</sup>A. J. Peace and N. Riley, "A viscous vortex pair in ground effect," *J. Fluid Mech.* **129**, 409–426 (1983).
- <sup>46</sup>J. D. A. Walker, C. R. Smith, A. W. Cerra, and T. L. Doligalski, "The impact of a vortex ring on a wall," *J. Fluid Mech.* **181**, 99–140 (1987).
- <sup>47</sup>J. J. Allen and M. S. Chong, "Vortex formation in front of a piston moving through a cylinder," *J. Fluid Mech.* **416**, 1–28 (2000).
- <sup>48</sup>G. Ovando, H. Juárez, G. Huelsz, and E. Ramos, "Vortex formation in a cavity with oscillating walls," *Phys. Fluids* **21**, 024101 (2009).

<sup>49</sup>J. Zhu, L. E. Holmedal, H. Wang, and D. Myrhaug, "Vortex dynamics and flow patterns in a two-dimensional oscillatory lid-driven rectangular cavity," *Eur. J. Mech. B: Fluids* **79**, 255–269 (2020).

<sup>50</sup>L. Wang, C. Guo, and Y. Su, "Numerical analysis of flow past an elliptic cylinder near a moving wall," *Ocean Eng.* **169**, 253–269 (2018).

<sup>51</sup>C. Norberg, "Fluctuating lift on a circular cylinder: Review and new measurements," *J. Fluids Struct.* **17**, 57–96 (2003).

<sup>52</sup>C. Lei, L. Cheng, S. W. Armfield, and K. Kavanagh, "Vortex shedding suppression for flow over a circular cylinder near a plane boundary," *Ocean Eng.* **27**, 1109–1127 (2000).